Delft University of Technology

Solute-induced transition in Poisson's ratio and strength
A phenomenon in additively manufactured Al-Si-Mg alloys

Ghoncheh, M. H.; Asgari, A.; Amirkhiz, B. Shalchi; Langelier, B.; Hadadzadeh, A.; Lloyd, A.; Mohammadi, M.

DOI
10.1016/j.matchar.2024.114384

Publication date
2024

Document Version
Final published version

Published in
Materials Characterization

Citation (APA)
Ghoncheh, M. H., Asgari, A., Amirkhiz, B. S., Langelier, B., Hadadzadeh, A., Lloyd, A., & Mohammadi, M. (2024). Solute-induced transition in Poisson's ratio and strength: A phenomenon in additively manufactured Al-Si-Mg alloys. *Materials Characterization*, *217*, Article 114384. https://doi.org/10.1016/j.matchar.2024.114384

Materials Characterization 217 (2024) 114384

Contents lists available at ScienceDirect

Materials Characterization

journal homepage: www.elsevier.com/locate/matchar

Solute-induced transition in Poisson's ratio and strength: A phenomenon in additively manufactured Al-Si-Mg alloys

M.H. Ghoncheh [a,*], A. Asgari [b], B. Shalchi Amirkhiz [a,c], B. Langelier [d], A. Hadadzadeh [e], A. Lloyd [f], M. Mohammadi [a]

[a] Marine Additive Manufacturing Centre of Excellence, University of New Brunswick, Fredericton, NB E3B 5A1, Canada
[b] Department of Maritime and Transport Technology, Delft University of Technology, Mekelweg 2, 2628 CD Delft, Netherlands
[c] CanmetMATERIALS, Natural Resource Canada, 183 Longwood Rd South, Hamilton, ON L8P 0A5, Canada
[d] Canadian Centre for Electron Microscopy, McMaster University, 1280 Main Street West, Hamilton, ON L8S 4M1, Canada
[e] Department of Mechanical Engineering, University of Memphis, Memphis, TN 38152, USA
[f] Department of Civil Engineering, University of New Brunswick, Fredericton, NB E3B 5A1, Canada

ARTICLE INFO

Keywords:
Laser powder bed fusion (LPBF)
Rapid solidification
AlSi10Mg
Solute partitioning
Finite element analysis
Stress triaxiality

ABSTRACT

In this study, cubic coupons of AlSi10Mg alloy were printed using the laser powder bed fusion (LPBF) technique. The effect of heating/reheating cycles on solute trapping and partitioning of alloying elements was investigated using atom probe tomography and transmission electron microscopy. Nano-hardness analysis and uniaxial tensile tests equipped with digital image correlation were employed to investigate the mechanical properties and Poisson's ratio. X-ray micro-computed tomography was utilized to detect strain localization sites along the building direction. Also, the uniaxial tensile test was simulated using finite element analysis to verify the experimental data and predict stress triaxiality. The results showed that the solute trapping and partitioning during the LPBF process results in remarkable changes in phases, their size and morphology, Poisson's ratio, strengthening factor, and consequently mechanical properties. While the tensile sample from top part of the LPBF coupon mostly shows porosity due to floating and entrapment of gases during layer-by-layer fusion/solidification, the sample from bottom part is exposed to sub-surface microcracking induced by residual stresses. The hardness, elastic, and shear moduli, Peierls stress, and cumulative strain energy of the top-part sample are higher than those of the bottom-part sample even though electron backscatter diffraction analyses report similar grain size and texture. Besides, by distancing from the build plate, the Poisson's ratio decreases. Simulation results of both samples indicate that the middle of the gauge is a high-potential area of failure initiation, where the bottom-part sample shows higher stress localization.

1. Introduction

Rapid solidification refers to high solid/liquid interface velocity (R) in a solidifying alloy that results in many practical potentials *e.g.,* fine microstructure, new metastable phases, segregation-less crystals, and increased solubility in solid state [1]. The cooling rate ($\dot{T}$) applied during rapid solidification processing (RSP) is within 10^5–10^6 K/s, which is achievable during laser powder bed fusion (LPBF) of some alloys [2–4]. The LPBF as an additive manufacturing (AM) technique employs a high-power laser to fuse the metal powder according to a 3-dimensional design. The product experiences high temperature gradients (G) at both macro-scale, *i.e.,* along the building direction, and micro-scale, *i.e.,* within each melt pool, where the first one determines the degree of AM component distortion and structural defects, while the second one mostly controls the microstructure morphology [5–8].

During RSP, a synergy between high R values and inadequate diffusion time of alloying elements due to extreme $\dot{T}$ leads to a steep deviation of solidification from the equilibrium condition. Consequently, the solute atoms are more prone to entrapment in the crystal lattice (*i.e.,* solute trapping or banding effect), showing less tendency of micro-segregation [9]. However, laser scanning on fresh powder layers leads to partial melting of the solidified layers underneath, resulting in repartitioning of solute atoms [10]. It can be postulated that a decrease in G from the bottom to the top of the printed coupon is responsible for both sample defects (*i.e.,* distortion, and cracking) due to residual

---

* Corresponding author.
E-mail address: mghonche@unb.ca (M.H. Ghoncheh).

https://doi.org/10.1016/j.matchar.2024.114384
Received 18 January 2024; Received in revised form 1 September 2024; Accepted 14 September 2024

Nomenclature

$\sigma_0,\sigma_P,\sigma_{SS},\sigma_{Pr},\sigma_{Dis},\sigma_{GB}$	Lattice, Peierls, solid solution, precipitation, dislocation, and grain boundary strengthening
$\sigma_{YS},\sigma_{UTS},s$	True yield stress, true ultimate tensile stress, and engineering stress
ε,e	True strain, and engineering strain
k_d	Locking parameter
D	Mean grain size
P_e	Peclet number
V_D	Diffusive speed
a_0	Constant on the order of interatomic spacing
D_L	Diffusion coefficient in liquid
R	Solid/liquid interface velocity
G	Temperature gradient
k_0,k',k_R,k'_R	Equilibrium, effective, R-dependent, and effective R-dependent partitioning coefficients
k	Strain coefficient
n	Strain-hardening exponent
ϑ	Poisson's ratio
E,μ	Elastic and shear moduli
H,φ,χ	Constants
C_i	Concentration of element i
d, b	The distance between slip planes, and the burgers vector
Y	Peak residual stress
Q_B	Heat input per unit build volume
H_M	Enthalpy of melting
α,α_0	Thermal diffusivity, and reference thermal diffusivity
β	Thermal expansion coefficient
$\Delta T = T_M - T_P$	Difference between melting temperature and preheat temperature
d_T	Track length
d_L	Laser spot diameter
T_A,T_P	Ambient temperature, and preheat temperature
P	Laser power
v	Scanning speed
t	Layer thickness

thermal stresses and phase variation (*i.e.,* composition, size, and morphology) due to a difference in solute trapping/repartitioning severity along the building direction [11,12]. Both can have considerable roles in the mechanical behavior of the alloy by determining the structural integrity and strain hardenability.

Extensive research has been conducted on the influence of AM on the mechanical properties of AlSi10Mg alloys [13–15]. These studies reveal that the SLM process, characterized by rapid solidification and directional cooling, significantly alters the microstructure of AlSi10Mg compared to conventional casting methods. The fine, lamellar microstructure typical of cast Al-Si alloys transforms into a unique, highly refined structure in LPBF parts. This transformation results in mechanical properties that often surpass those of traditionally cast counterparts [15]. For instance, LPBF AlSi10Mg parts exhibit higher ultimate tensile strength and Vickers hardness than high-pressure die-cast AlSi10Mg [13,15]. Additionally, the elongation at break for LPBF parts can be comparable or even superior, particularly in the horizontal build direction [13,15]. These findings underscore the potential of LPBF to enhance the performance of AlSi10Mg components in various applications, driven by the fine microstructure achieved through this advanced manufacturing technique.

During LPBF, the solidifying material undergoes $G \approx 10^5 - 10^{7^\circ} C/m$, and $R \approx 0.1\ m/s$ [9]. While G/R ratio is mostly used to identify the grain morphology (*i.e.,* cellular, columnar-dendritic, and equiaxed), the factor $G \times R$ or $\dot{T}$ determines the grain size in as-built structure [16]. High-strength properties of an LPBF part are usually attributed to its fine microstructure; however, according to the total theoretical strengthening equation (Eq. (1)), the impacts of the individual strengthening mechanisms, *i.e.*, precipitation strengthening (σ_{Pr}), dislocation strengthening (σ_{Dis}), and grain boundary strengthening (σ_{GB}), cannot be overlooked [17,18].

$$\sigma_{YS} = \sigma_0 + \sigma_{Pr} + \sigma_{Dis} + \sigma_{GB} \tag{1}$$

The effect of the first term (lattice stress or σ_0) is usually neglected, while this can remarkably contribute to the mechanical properties of an LPBF product. The term σ_0 in Eq. (1) can be separated to that of the Peierls stress (σ_P) and the solid solution strengthening (σ_{ss}), and can be written as follows [19,20]:

$$\sigma_{YS} = \sigma_P + \sigma_{SS} + \sigma_{Pr} + \sigma_{Dis} + k_d D^{-0.5} \tag{2}$$

in which k_d and D respectively refer to the locking parameter and the mean grain size. The variations in the chemical content of the AM hybrid AA2618/AlSi10Mg have considerable impact on σ_P and σ_{SS}, which can expand to a single alloying system based on the concept of solute trapping [10]. In terms of σ_{Pr}, it has been reported that although the LPBF AlSi10Mg shows various precipitates with both coherence and incoherence interfaces, precipitate strengthening interpreted by the Orowan mechanism applies negligible difference in mechanical properties along the building direction [21]; however, in this study, the role of σ_{Pr} in the mechanical properties of the LPBF AlSi10Mg will be proven as the undeniable and remarkable factor. Apart from that, the dislocation density in the as-built structure is reported to be high ($\approx 10^{14} - 10^{15}\ 1/m^2$) regardless of the distance from the build plate [12,22]. In addition, the cell spacing does not change along the building direction; thus, the variation of σ_{Dis} through the building direction can also be insignificant [23]. All corroborates the undeniable importance of σ_0 on the mechanical properties of LPBF AlSi10Mg, all while the role of σ_{Pr} should be disclosed that will be interpreted in this study.

The aim of this study is to investigate the uniaxial tensile behavior and the Poisson's ratio of an LPBF AlSi10Mg alloy, which are surprisingly affected by moving upward through the building direction. To this, the effect of heating/reheating cycles on solute trapping, phase formation, strengthening mechanisms, and structural defects is investigated in the material. Subsequently, the uniaxial tensile behavior of the material associated with analysis of strain hardenability and strain localization contours is discussed. In the end, the interconnections between the microstructural characteristics analyzed using advanced electron microscopy analyses and the mechanical response of the material experimented and simulated are interpreted.

2. Material and methods

2.1. Material and manufacturing process

AlSi10Mg powder with a size distribution of 10–45 μm was supplied by EOS GmbH to be used as material feedstock for AM processing. To process the AlSi10Mg coupons, an EOS M290 laser powder bed fusion (LPBF) additive manufacturing machine equipped with a 400 W Yb-fiber laser and spot size of 100 μm was employed. 67°-rotation stripe scanning pattern between consecutive layers was used so that the build plate temperature, laser power, scanning speed, hatching distance, and powder layer thickness were set on $200^\circ C$, 370 W, 1300 mm/s, 190 μm, and 30 μm, respectively. Cubic coupons with dimensions of $10 \times 20 \times 40\ mm^3$ were vertically printed at track length of $8 \pm 0.5\ mm$, and chemically analyzed using the inductively coupled plasma-optical emission spectroscopy (ICP-OES) method. The chemistry of the printed samples randomly analyzed is presented in Table 1.

An electrical discharge machine (EDM) was used to produce two sets of miniature dog-bone tensile samples with dimensions given in Fig. 1. One set of samples was prepared from the top and one set from the bottom part of the printed cube. In total, 3 uniaxial tensile samples were manufactured for each set to ensure repeatability of the results. The samples were cut in such a way that building direction was perpendicular to load direction during the uniaxial tensile testing. This was to assess the mechanical behavior of the material through an axis perpendicular to the building direction, as they usually show elongated coarse grains along the building direction that might cause mechanical weakness through another directions [21]. To pull up the tensile samples, a machined plain-steel fixture was manufactured to fit the samples, as shown in Fig. 1.

2.2. Characterization techniques

The LPBF sample with 2 *mm* thickness was ion milled using a Gatan 691 PIPS to prepare TEM samples. To observe the distribution of alloying elements in the matrix, an FEI Tecnai Osiris transmission electron microscope (TEM) with a 200 *keV* X-FEG gun was used. For EDS elemental mapping, a sub-nanometer electron probe was employed. Atom probe tomography (APT) was performed *via* a local electrode atom probe (LEAP) 4000× HR equipped with a reflection. To prepare the samples, an NVision 40 dual beam instrument to assist with lifting of the samples was utilized. An ultra-high vacuum of 4×10^{-11} *Torr* and a low temperature of $\sim 60\,K$ were applied during the test, where UV laser pulses with 355 *nm* wavelength, 60 *pJ* pulse energy, and 125–250 *kHz* pulse frequency were also used to facilitate field evaporation. The detection rate of the target was set at 0.005 ions per pulse (0.5 %) and controlled *via* changing the DC voltage passed through the APT samples. Both the chosen base temperature and laser operation mode were intended to maximize data acquisition from the fine microstructure of the LPBF material. These parameters fall comfortably within standard operational ranges for the APT analysis of such materials. Any potential errors arising from surface diffusion induced by laser exposure for substitutional solutes are generally negligible compared to the observed precipitate sizes in the samples and the concentration thresholds (3 at. %) used to identify these precipitates from the voxelized data. Besides, electron backscatter diffraction (EBSD) technique was employed along the building direction to study the grain structure of the AM coupons through the unique grain maps, where the machine was equipped with a field emission gun scanning electron microscope (FEGSEM) with a step size of 0.3 μm.

X-ray micro-computed tomography (Micro-CT) was conducted to detect internal defects of the LPBF samples before tensile testing. Two CT modes of maximum intensity projection (MIP) and attenuation were employed to reveal inclusions and porosity/crack in the samples. A Skyscan 1072 Micro-CT apparatus with an X-ray tube set on 90 $kV/110\ \mu A$ was used. Over a 360° rotation of the sample, 8 frames were acquired with 9968 *ms* acquisition time and averaged at each 0.9° during image collection process. The resolution of images was 10.9 $\mu m/pixel$. Skyscan NRECON and Skyscan CTVox were used for reconstruction and visualization, respectively.

2.3. Mechanical testing

Six miniature tensile samples (three per part) were uniaxially tested at strain rates of $6.9(\pm 0.5) \times 10^{-4}\ s^{-1}$ using an INSTRON-5985 universal apparatus with a 25-*mm* extensometer. To plot the actual strain contours of the necking area during the deformation, digital image correlation (DIC) technique was employed using a VIC-2D system by correlated solutions. To compare data between top and bottom parts, 8 instances on the stress-strain curve were selected.

To measure the elastic modulus and the hardness of LPBF AlSi10Mg tensile samples, an iMicroTM Nanoindenter with a Diamond-Berkovich indenter was used. A 2-by-5 rectangular pattern was set over two areas on the gauge length of samples cut from each part. Also, $0.1(\pm 0.01)\ s^{-1}$ and 50 *mN* were chosen as the strain rate and maximum load, respectively.

3. Simulation

To model the stress and strain distribution in the samples along with stress triaxiality close to the necking area, a 3D simulation was accomplished using the commercial finite element package ABAQUS/Standard version 6.20 with an implicit integration scheme. The sample geometry along with the prescribed boundary conditions and meshes are shown in Fig. 2. The samples' geometry and size were chosen for the modeling in a way to replicate the uniaxial tensile samples.

A reference point was set on the top of tensile sample model to apply the corresponding displacement, where the reference point was coupled with the upper part of the model. The bottom of the tensile test model was fully clamped, while its top was subjected to a degree of freedom to be displaced only vertically. Some partitions were added to the model to have finer meshes over the gauge area through which the stress was concentrated, and coarse meshes on the areas far away from the center. As mesh size can influence the output directly, a mesh convergence study was accomplished. Finally, the model comprises 8178 brick elements including 6978 elements C3D8R and 1200 elements C3D20R. In the pursuit of achieving the most accurate representation of a tensile test simulation, a distinction was made in the type of elements employed within the region under the grip zone. A standard boundary was established between two dissimilar element types, effectively leading to the segmentation of the tensile sample and the subsequent definition of two distinct element categories.

Results of modeling, force-displacement, were verified with experiments to make the prediction of responses accurate. Outputs such as force and displacements were extracted from the reference point. The results were compared with the stress-strain curves obtained numerically for calibration purposes. In addition, the contours of equivalent plastic strain and von Mises stress were extracted from the simulation for both the top and bottom samples. The DIC images mainly close to the necking area were used to validate the simulation framework. Finally, the stress triaxiality was measured for the whole gauging area and further discussed and compared for the necking areas of the top and bottom samples.

4. Theory

4.1. Solute partitioning during rapid solidification

The ease of solute rejection during solidification depends on many thermophysical factors such as diffusion coefficient of solute atoms in

Table 1
Chemical composition of the AlSi10Mg samples.

Element (Wt%)	Si	Mg	Fe	Mn	Cu	Ni	Zn	Ti	Al
AlSi10Mg	10.0	0.33	0.55	≤ 0.45	≤ 0.05	≤ 0.05	≤ 0.1	≤ 0.15	Bal.

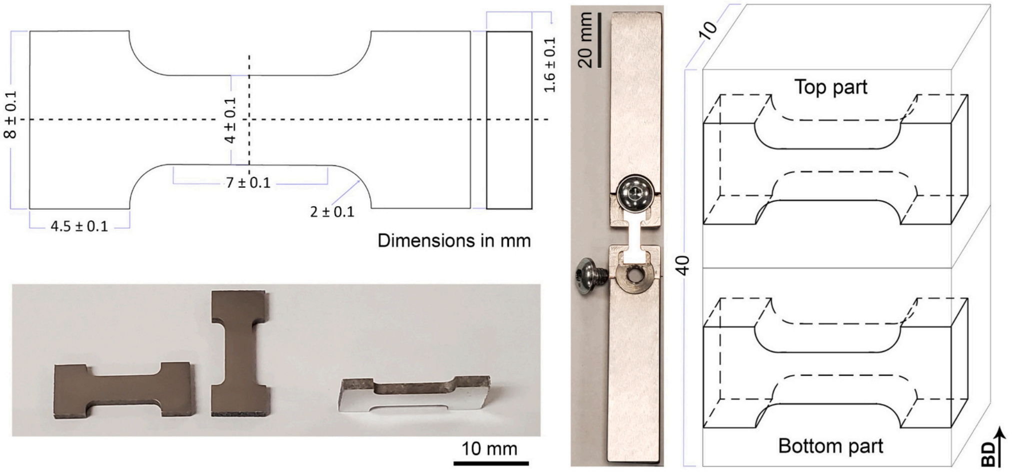

Fig. 1. Layout of printed coupons, tensile samples, fixture, and corresponding dimensions.

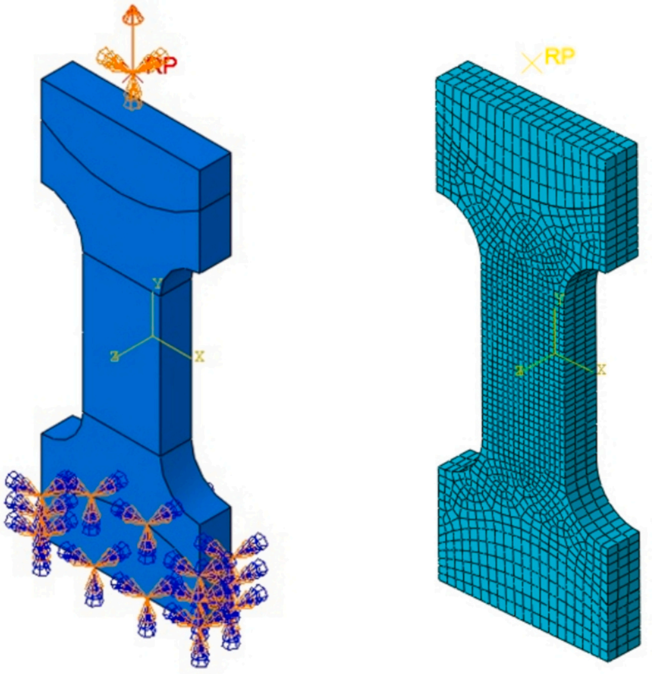

Fig. 2. Schematic of the modeling framework including boundary conditions, partitions, and meshes.

liquid, solidification front velocity, the interatomic spacing, and natural convection within the solidifying melt. While the term "equilibrium partitioning coefficient" or ($k_0 = C_S/C_L, 0 \le k_0 < 1$), is simply used to determine the solute rejection tendency (C_S and C_L refers to the composition in solid and liquid phases), considering the impact of various factors under non-equilibrium condition needs more formulations. In hypoeutectic aluminum alloys, the alloying elements with lower k_0 basically tends to be rejected more ahead of solidification front [16]. During the LPBF, the fused powder layers experience rapid solidification usually introduced by no diffusion in solid and partial diffusion in liquid phase [9]. At high solid/liquid interface velocity (R) during the rapid solidification, partitioning coefficient drifts away from k_0 and even approaches unity at severe R values [24]. The R-dependent partitioning, also called (k_R), can be written as:

$$k_R = \frac{k_0 + Pe}{1 + Pe}, Pe = \frac{R}{V_D} \quad \text{and} \quad V_D = \frac{D_L}{a_0} \tag{3}$$

where (Pe) and (V_D) are the Peclet number and the diffusive speed, while (a_0) and (D_L) refer to a constant on the order of interatomic spacing and the diffusion coefficient in liquid phase. a_0 and R are reported as $10^{-9}\ m$ and $10^{-2}\ m/s$, respectively [25].

Natural convection applied by the thermocapillary forces or the Marangoni effect through a melt pool considerably plays a role in distribution of solute during solidification [10,16]. In presence of natural convection, *e.g.,* LPBF process, the partitioning coefficient further deviates from k_0 by applying a correction factor given in Eq. (4). The term "effective partitioning coefficient" or (k') refers to this condition as follows [9]:

$$k' = \frac{k_0}{k_0 + (1 - k_0)e^{(-R\delta/D_L)}}, 0 \le k_0 \le k' \le 1 \quad \text{and} \quad 0 \le \delta < \delta_L \tag{4}$$

here ($\delta_L = D_L/R$) is the diffusion length ahead of solidification front that is subjected to constitutional undercooling due to solute rejection. In the LPBF, inadequate time for solute rejection due to high R values lead to shorten the diffusion length such that δ_L limits to δ [9]. An interplay between rapid solidification and natural convection during this process introduces the following:

$$k'_R = \frac{k_0 D_L + a_0 R\chi}{\chi(D_L + a_0 R)}, \chi = k_0 + \frac{1 - k_0}{e} \tag{5}$$

which is derived by substituting Eq. (4) in Eq. (3). This derivation has been discussed with more details elsewhere, see [9,10].

4.2. Mechanical response and strengthening factors

The tensile data achieved by the uniaxial tensile test was an engineering stress-strain type, which does not provide a true indication of the material flow under uniaxial tensile loading. Since the specimen dimensions continuously change during the test, the true stress-strain, or flow curve, is a better approach to present the deformation manner of the alloy; however, some considerations are required to correlate the engineering stress-strain and the flow curve data. Within the homogenous plastic deformation (*i.e.,* between the onset of yielding and the maximum load), the Hollomon parabolic relation can be generally written as follows [26]:

$$\sigma = k\varepsilon^n, \sigma = s(1 + e) \quad \text{and} \quad \varepsilon = ln(1 + e) \tag{6}$$

in which (σ) and (s) are true and engineering stresses, respectively, and (ε) and (e) are their corresponding strains. (k) and (n) are also named as the strain coefficient and the strain-hardening exponent, respectively. While n is the slope of the $ln\sigma - ln\varepsilon$ plot, its dependency on the solute distribution through the matrix is of interest, as is discussed in this study.

Regarding different strengthening factors which impact on the tensile strength of the material, the lattice friction, which acts as an obstacle against the planar dislocation's movement can be roughly determined by a continuum model first presented by Peierls [27] and it is written as

$$\sigma_P \approx \frac{2\mu}{1-\vartheta} exp\left(\frac{-2\pi}{1-\vartheta}\frac{d}{b}\right) \tag{7}$$

As shown in Eq. (7), the magnitude of the Peierls stress (σ_P) for the planar dislocations is dependent on the shear modulus (μ), the distance between slip planes (d), and the Burgers vector (b). In this regard, μ can be directly calculated as follows [27].

$$\mu = \frac{E}{2(1+\vartheta)} \tag{8}$$

where (E) is the elastic modulus and (ϑ) is the Poisson's ratio in a random texture. These two values can be calculated from the nano-indentation tests and information from the available literature.

The solid solution strengthening increment (σ_{SS}) is defined by Eq. (9) in which (H) and (φ) are constants, while (C_i) is the concentration of element i in the matrix. The constant φ is reported as $2/3$ [28,29]. As will be explained, Si mostly prefers to either precipitate individually with negligible contribution to solid solution strengthening, or react with Mg to form (Mg,Si)-bearing phase that is impactful for this strengthening mechanism. Si atoms that do not form the individual Si phase are assumed to only react with Mg to form (Mg,Si)-bearing phase. Under this circumstance, Eq. (9) can be rewritten as Eq. (10) in which $H_{(Mg,Si)_{eq}}$ is $39.7\ MPa/(Wt.\%Mg)$ [28,29].

$$\sigma_{SS} = H_{Mg}C_{Mg}^{\varphi} + H_{Si}C_{Si}^{\varphi} \tag{9}$$

$$\sigma_{SS} = H_{(Mg,Si)_{eq}}C_{Mg}^{\varphi} \tag{10}$$

4.3. Residual stresses

To measure the part-scale peak residual stresses through the thickness of a vertically printed metallic component, an analytical model was recently developed [30]. According to Buckingham π-theorem, process parameters, thermophysical and mechanical properties of the AM material are reported as influential factors on the peak residual stresses through the building direction, as given below [30]:

$$\pi_1 = f(\pi_2, \pi_3, 1/\pi_4\pi_5, 1/\pi_6); \tag{11}$$

$$\pi_1 = Y/\sigma_{YS};\quad \pi_2 = Q_B/H_M;\quad \pi_3 = \beta\Delta T;\quad \pi_4 = T_P/T_A;\quad \pi_5 = d_T/d_L;\quad \pi_6 = \alpha/\alpha_0$$

Subsequently, the peak residual stress (Y) can be written as below in which the thermophysical properties of the AM AlSi10Mg are given in Table 2. Also, the parameters (P), (v), (h), (t), (d_T), (d_L), and (T_P) used in this study were previously reported in the section 2.1, while (α_0) is considered as the thermal diffusivity of pure aluminum.

$$Y/\sigma_{YS} = 0.5124\left[\frac{(Q_B/H_M)(\beta\Delta T)\sqrt{d_T/d_L}}{(T_P/T_A)\sqrt{\alpha/\alpha_0}}\right]^{0.6403}; Q_B = P/vht,\quad \Delta T = T_M - T_P \tag{12}$$

5. Results

5.1. Solute partitioning and formation of precipitates

Fig. 3 shows the top-view (x-y plane) STEM-BF images, *i.e.,* the TEM images obtained in the scanning mode (STEM) using a bright field detector (BF), and the corresponding EDS elemental maps of the LPBF AlSi10Mg from foil samples extracted from both top and bottom parts. The analyses were collected far away from the cell boundaries to investigate the phases embedded in the matrix. In the micrograph representing the top-part microstructure, there are some features such as individually grown Si precipitates (point i), very fine spherical (Mg,Si)-bearing phase (point ii), and Mg solute clusters trapped in the matrix (point iii). On the other side, the sample representing the microstructure of the bottom part presents no individual Si precipitates, low fraction of Mg solute clusters trapped in the matrix (point iii), and some elongated lamellae containing Si and Mg solutes formed in various directions called as (Mg,Si)-bearing phase (points iv and v). Diffusivity and equilibrium partitioning of Si and Mg in the liquid Al are tabulated in Table 3 [31–34]. Inserting these data in Eq. (^{5}) gives the solute partitioning in the presence of rapid solidification and natural convection presented here as well. Comparing k_0 and k'_R reveals that the aforementioned factors result in an increase in reluctance of solute segregation as the partitioning coefficients receive higher values.

Looking at the bright-field STEM micrographs in Fig. 4, both the average cell size and the morphology of them are quite comparable between the top and bottom parts. To measure the cell size in the structure of L-PBF-AlSi10Mg material, the cells' diameters were measured using the line intercept method and image processing technique. The consistent cell size along the build direction suggests that the cooling conditions throughout the building process were fairly uniform. The negligible variations in cell size by distancing from the build plate, coupled with the unchanged cell structure and morphology that both show a "fish scale" pattern in the L-PBF-AlSi10Mg material indicate that the repeated thermal cycles did not significantly alter the dendritic/cell structure of the material. Apart from that, the STEM-Bright field at higher magnifications are also shown in Fig. 4, where both samples show an interconnected eutectic Si phase nucleated at intercellular regions and formed the eutectic walls.

5.2. Phase evolution and grain structure through the building direction

3D APT maps of a narrow area collected far away from the cell boundaries and the associated concentration variation profiles are presented in Fig. 5. The APT map from a specimen extracted from the top part of the sample shows several coarse precipitates defined by Si isoconcentration surfaces (green color) with sharp edges, and a higher number of spherical precipitates defined by Mg isoconcentration surfaces (purple color). Proximity histograms from select isoconcentration surfaces reveal concentration profiles showing that the blocky precipitates are solely formed by Si atoms, while the spherical ones contain Mg and Si atoms with the atomic ratio of Mg:Si (~1:1). On the other side, the APT map from a specimen extracted from the bottom part of the sample illustrates very low fraction of Si precipitates, and (Mg,Si)-bearing phases with both spherical and rod-shape morphologies that are coarser than the ones in the top-part sample. The concentration profiles present the same ratio between Mg and Si contents. The solute content in

Table 2
Thermophysical properties of the LPBF AlSi10Mg [30], and the process parameters used in this study.

Parameter	$Q_B(\times 10^7)$ (J/m^3)	$H_M(\times 10^6)$ (J/m^3)	$\beta(\times 10^{-6})$ (K^{-1})	$\alpha(\times 10^{-6})$ (m^2/s)	$\alpha_0(\times 10^{-6})$ m^2/s	T_P (K)	T_M (K)	T_A (K)	$d_T(\times 10^3)$ (μm)	d_L (μm)
Magnitude	4990	2776	23.0	43.95	83.0	473 ± 5	868	298	8.0 ± 0.5	100

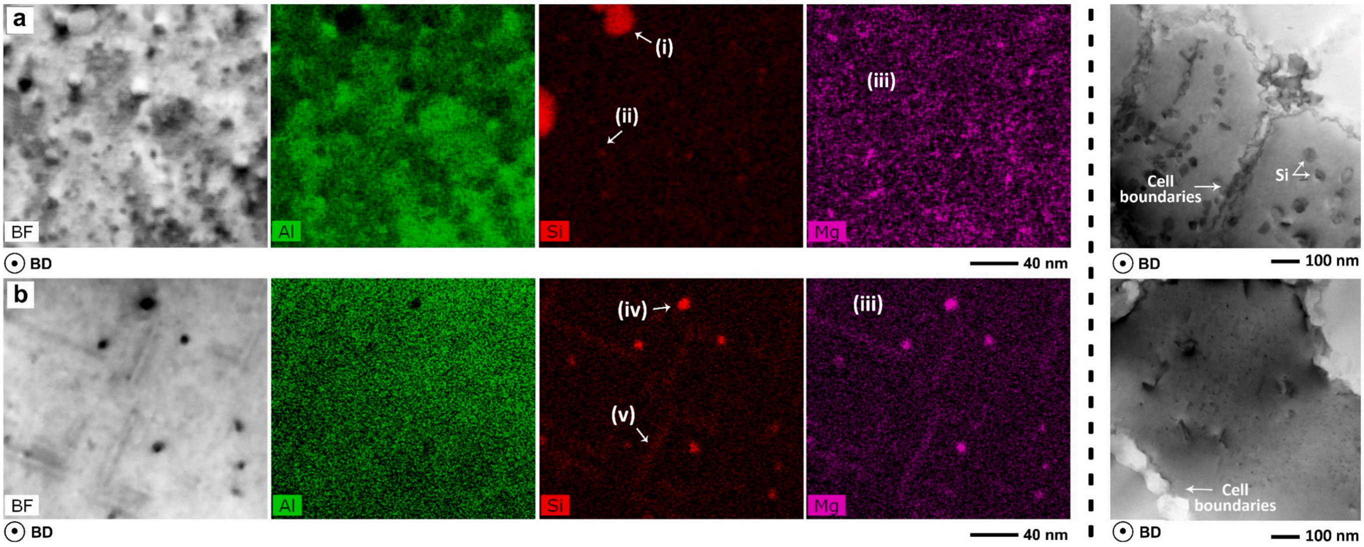

Fig. 3. The STEM-BF micrographs and the corresponding elemental distribution maps of (a) top part, and (b) bottom part of the LBPF AlSi10Mg coupon (BD: building direction).

Table 3
Physical properties of the solute rejected during solidification of AlSi10Mg alloy.

Element	a_0 (mm)	D_L (m^2/s)	k_0 in liquid Al	k'_R in liquid Al
Mg	10^{-9}	5.8×10^{-9}	0.3	0.54
Si	10^{-9}	9.2×10^{-9}	0.13	0.29

the APT maps is reported in Table 4.

According to Fig. 6, the unique grain color maps of undeformed samples indicate that the AM AlSi10Mg coupon shows similar grain structure in both parts containing elongated columnar grains among which some epitaxially grew along the building direction and equiaxed grains mostly formed within top middle parts of each melt pool. The corresponding pole figures also reveal a quite similar grains orientation in both samples. Considering an individual melt pool, the formation of columnar grains at melt pools' boundary is due to the dominance of G in G/R. The nucleation of equiaxed grains, on the other side, is attributed to solute rejection ahead of the growing columnar grains that subsequently increases the solute concentration in the liquid and provides a sufficient level of constitutional undercooling, *i.e.*, solute enrichment in the liquid ahead of an advancing solid front can trigger nucleation on available substrate particle, to nucleate the equiaxed grains. This is due to a decrease in the term G/R, as R value increases. Apart from that, the Marangoni effect also plays the other important role in the formation of equiaxed grains by applying shear forces to the grown columnar grains. The shear force can break the tip of columnar grains, letting them float into the liquid. These small particles can act as heterogenous nucleation sites so that the high frequency of these potential sites accompanied by the constitutional undercooling led to the formation of the equiaxed grains. The average grain size (*i.e.*, grain area) in the top-, and bottom-part samples are reported as 803 ± 6 and 841 ± 11 μm^2, (respectively)

5.3. Peierls stress and other strengthening factors

The nanoindentation analysis was used to measure the elastic modulus and the hardness, where the mean values were achieved from 10 measurements on each part. As mentioned in Eq. (^{8}), the elastic modulus of the printed alloy can be used to measure the shear modulus. μ values presented in Table 5 are obtained considering 0.319 ± 0.007 and 0.374 ± 0.004 as the Poisson's ratio of the top and bottom parts, respectively. These values were calculated *via* the DIC-assisted tensile tests presented in Section 5.5. According to the literature, the Burgers vector, b, and the distance between slip planes, d, in the aluminum alloys are approximately 2.86 Å, and 4.05 Å, respectively, where d/b approaches its maximum magnitude of $\sqrt{2}$ [35,36]. Subsequently, the magnitude of the Peierls stress can be calculated based on the continuum model presented in Eq. (^{7}) and is reported in Table 6. The top-part sample shows higher hardness, elastic, and shear moduli, as well as the Peierls stress, which indicates that the friction force against the planar dislocations' mobility through the top part is higher [37].

As shown in the microstructural analyses, while the bottom part solely shows elongated (Mg,Si)-bearing phase, the top part shows both well-dispersed fine (Mg,Si)-bearing phase and Si-bearing precipitate. Regardless of those Si atoms that participate in Si-bearing precipitate formation, the rest reacts with Mg to form (Mg,Si)-bearing phase through both top and bottom parts. Hence, σ_{SS} can be measured *via* Eq. (^{10}) in which C_{Mg} is obtained from Table 4 (note that the concentration should be in weight percent). The role of the strengthening increments in total strength of each part is presented in Table 6, where the contribution of $(\sigma_{Pr} + \sigma_{Dis} + \sigma_{GB})$ can be measured using Eq. (^{2}) and σ_{YS} values reported in the section 5.5.

According to Fig. 7, it is apparent that the top part of the LPBF AlSi10Mg coupon exhibits a somewhat unremarkable increase in the steepness of its load-depth curve. This minor variation confirms a nearly identical trend in the rate of strain hardening for both samples. Moreover, at every level of loading, the indented region in the sample taken from the top part of LPBF AlSi10Mg displays shallower depths, attributed to higher hardness than in the bottom part. The nanoindentation test was conducted over a 2 × 5 rectangular pattern (30 μm spacing) on each part to make sure that the reported value can represent the average of hardness measurements at different places of the LPBF matrix.

5.4. X-ray micro-computed tomography (micro-CT)

Fig. 8 shows the micro-CT images of the undeformed tensile samples taken from both parts of the LPBF AlSi10Mg coupons at different time frames and two modes of MIP and attenuation. Three different samples taken from each part underwent micro-CT analysis to ensure the reproducibility and accuracy of the data. While both samples contain some inclusions that emerged as bright spots in the MIP mode (red circles), other structural defects seem to be different in nature from one side to another shown in the attenuation mode. Herein, the bottom part with relative density of 97.3 ± 0.4 % shows four micro-cracks nucleated

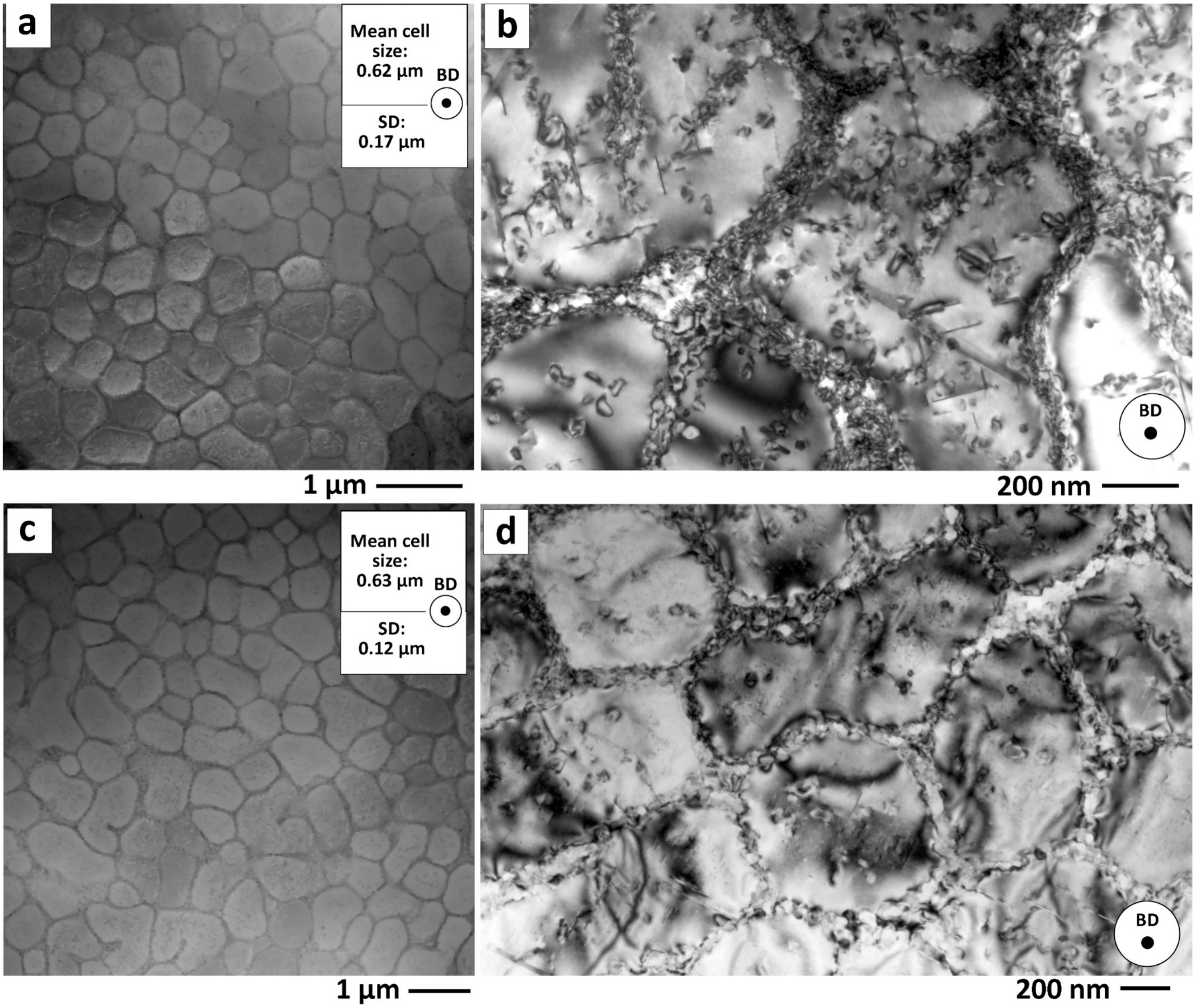

Fig. 4. The cellular structure and the intercellular regions as the nucleation sites of the eutectic Si phase in (a, b) top-part, and (c, d) bottom-part samples (note that the magnifications are not the same).

and propagated from the surface, but the top part with relative density of 98.6 ± 0.2 % only displays three pores and one micro-crack over the entire sample. While the presence of inclusions can be attributed to the entrance of contaminations during the powder fusion process, oxide formation and engulfment into a highly dynamic melt, the sources of micro-cracks and porosity formation can be due to many factors such as the melt viscosity, thermocapillary forces, residual stresses, gas entrapment, and alloying elements with different thermal expansion coefficients; this will be discussed in fair details ahead. Considering the residual stresses, Eq. ([12]) shows that this factor corresponds to the yield stress, *i.e.*, $Y_{AlSi10Mg} \approx 0.59\sigma_{YS}$, which means that Y as a representative factor of the residual stresses is approximately equal to 131.8 and 149.6 MPa for the bottom-, and top parts based on the data presented in next section (Table 7). The magnitudes of standard deviation are 1.3 MPa and 2.1 MPa, respectively. However, T_P in the top part can be different from the one in the bottom part due to consecutive heating/reheating cycles, and subsequently, the heat kept through the printed layers underneath, which applies a deviation in Y value of the top part. To avoid complexity, T_P is assumed constant through the LPBF component regardless of the distance from the build plate.

5.5. *Tensile properties and solute-induced strain hardening*

Fig. 9(a) shows the engineering stress-strain ($s - e$) curves accompanied by the DIC contours. Both top-part and bottom-part samples show an elastic-plastic tensile behavior in which the plastic zone mostly contains uniform plastic deformation, *i.e.*, negligible post-necking non-uniform deformation. Surprisingly, the sample from the top part presents better cumulative strain energy, where both tensile strength and total elongation have increased. Eq. ([6]) can be used to plot true stress-strain ($\sigma - \varepsilon$) curves thanks to a negligible post-necking plastic deformation, *cf.* Fig. 9(b). Dash lines in Poisson's ratio curves at very early stages of the tensile testing were drawn because of slight movements of specimens seating into the testing apparatus (fixtures and grips) with the application of load; however, this issue was resolved at further loading. Poisson's data was plotted by placing a virtual extensometer at approximately the mid height of the AM miniature tensile samples extending across nearly the full width and extracted transverse strain. This is divided by longitudinal strain to calculate the Poisson's ratio. As elucidated in Fig. 9(b), The Poisson's ratio for the bottom and top parts are reported as 0.374 ± 0.004 and 0.319 ± 0.007, respectively. Other advanced manufacturing techniques involving high cooling rates such as

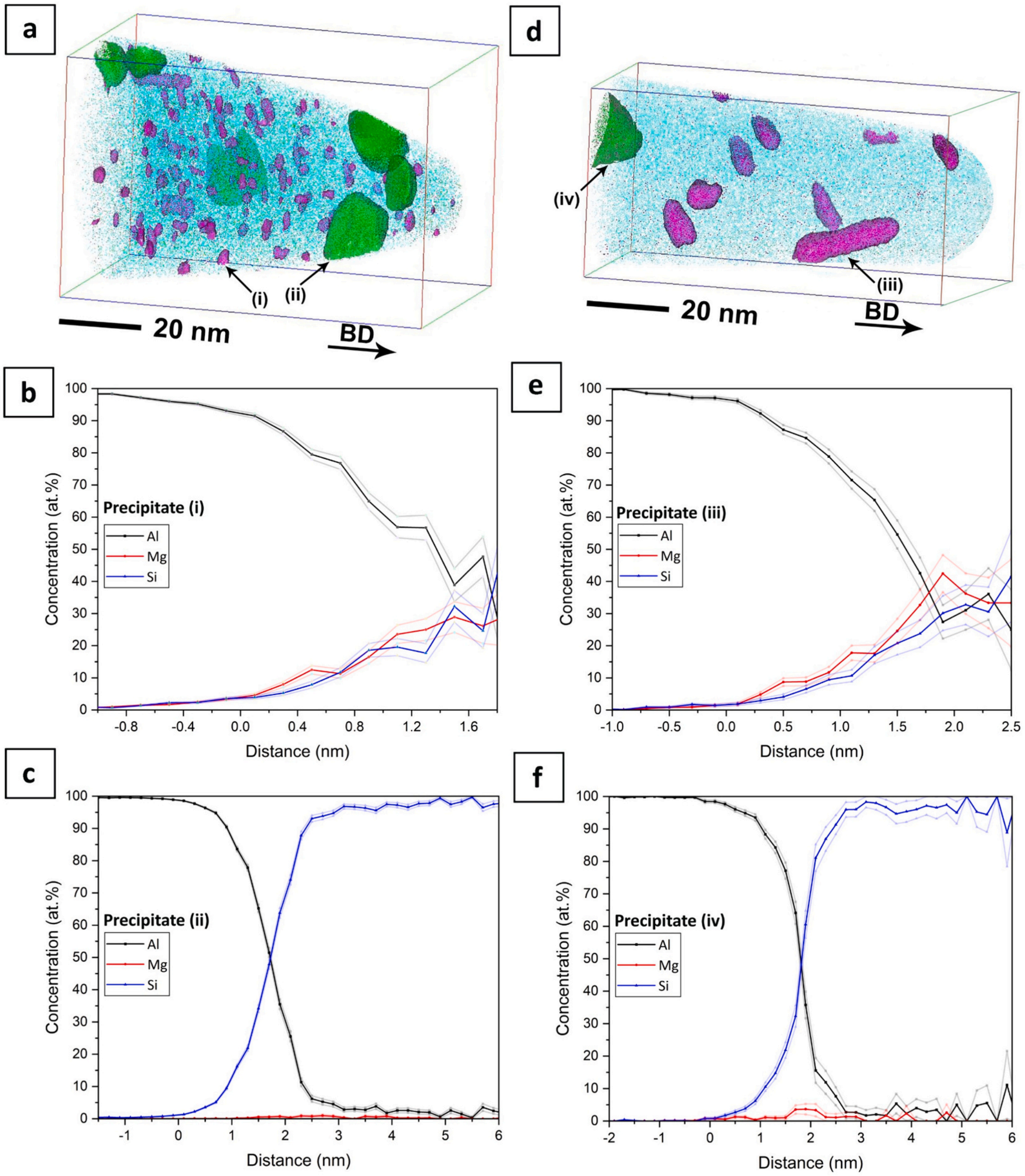

Fig. 5. (a,d) APT maps with precipitates identified using isoconcentration surfaces of 3 at.% Si (green) and 3 at.% Mg (purple), and (b,c,e,f) the proximity histograms showing the concentration-distance profiles of select precipitates (indicated i-iv) and absolute error of the concentration at each distance. APT datasets are obtained from (a-c) the top part, and (d-f) the bottom part of the LPBF AlSi10Mg coupon (BD: building direction).

Table 4
The concentration of alloying elements in the APT maps of LPBF AlSi10Mg.

Sample	Element (atom %)		
	Si	Mg	Al (+ trace)
Top part	0.635 ± 0.002	0.031 ± 0.001	Bal.
Bottom part	0.128 ± 0.003	0.038 ± 0.002	Bal.

laser cladding, laser surface modification, and laser material deposition can produce functionally graded microstructures that the change in Poisson's ratio cannot be negligible [38–40]. According to Fig. 9(c), Through the plastic deformation, both samples show very similar trends in flow behavior and $ln\sigma - ln\varepsilon$; however, the reason behind differences in samples' mechanical properties is still of particular interest. Table 7 presents the mechanical properties of the samples' tensile testing.

5.6. Simulation results

Experimental force-displacement data were used to verify the simulation results. As can be seen in Fig. 10, the simulation results of both bottom-part and top-part samples show great accordance with the experimental results reporting less than 5 % error. Right after the onset of necking, the samples experience failure; thus, the simulation is only focused on the areas prior to the ultimate stress point, *i.e.,* the post necking is neglected. There can be other mechanisms being active in that region, which is outside the scope of this study [41,42]. The material's constitutive models, regardless of being BP or TP, have two components relying on the plastic strains range which are presented in Table 8.

It is important to highlight that the material does not exhibit conventional mechanical behaviors, thus failing to satisfy Considère's theorem. According to Considère's theorem, the hardening exponent n value should correspond to the necking strain. However, if this term in LPBF AlSi10Mg is set to match a necking strain, the R-square value,

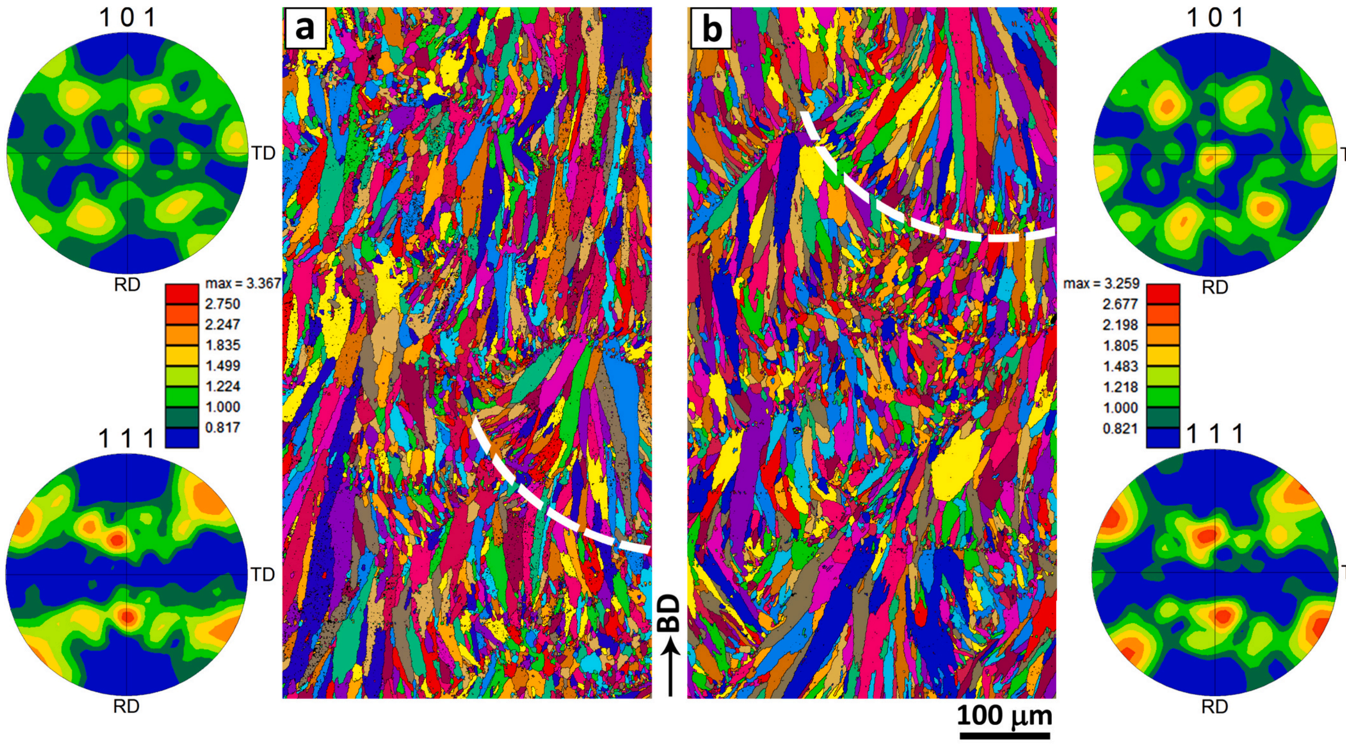

Fig. 6. Unique grain color maps and corresponding pole figures of the as-built structure through (a) the top part, and (b) the bottom part of printed material (white dash lines: melt pool boundaries).

Table 5
Physico-mechanical characteristics of the LPBF AlSi10Mg.

Sample	Hardness (***HV***) / SD*	***E*** (***GPa***) / SD	***μ*** (***GPa***) / SD
Top part	154 / 5	80.90 / 0.85	30.88 / 0.32
Bottom part	144 / 4	79.11 / 0.85	28.87 / 0.32

SD: Standard deviation.

Table 6
The contribution of different strengthening mechanisms in the LPBF AlSi10Mg.

Sample	σ_P (***MPa***) / SD*	σ_{SS} (***MPa***) / SD	$(\sigma_{Pr} + \sigma_{Dis} + \sigma_{GB})$ (***MPa***)
Top part	2.25×10^{-1} / 1.6×10^{-3}	32.87 / 0.70	218.10
Bottom part	0.67×10^{-1} / 1.6×10^{-3}	37.65 / 1.32	183.58

SD: Standard deviation.

which reflects the accuracy of the fit, decreases remarkably, a level that is insufficiently accurate and therefore unacceptable. A similar trend, not adhering to Considère's theorem, was reported by other researchers, as discussed in the final section of this study for comparison.

Applying the Von Mises yield criterion, Fig. 11 shows the Mises stress and the equivalent plastic strain through the tensile samples obtained from the finite element analysis in which the modeling was properly calibrated with the experimental results. Similar to the experiments, the areas under the screws did not experience any stress as no deformation was assumed at these locations. The most plastic strains are observed on the middle of the sample at which failure potentially happens. Regardless of the stress and strain magnitudes, both samples show very similar stress and strain distributions. The equivalent plastic strain of the bottom-part sample resulted from the simulation is about 0.0548, which is comparable to the experimental result of 0.059 and presents an acceptable error of 6.7 %. Also, a difference between the simulation and the experimental equivalent plastic strains in the top-part sample indicates an error of 4.4 %.

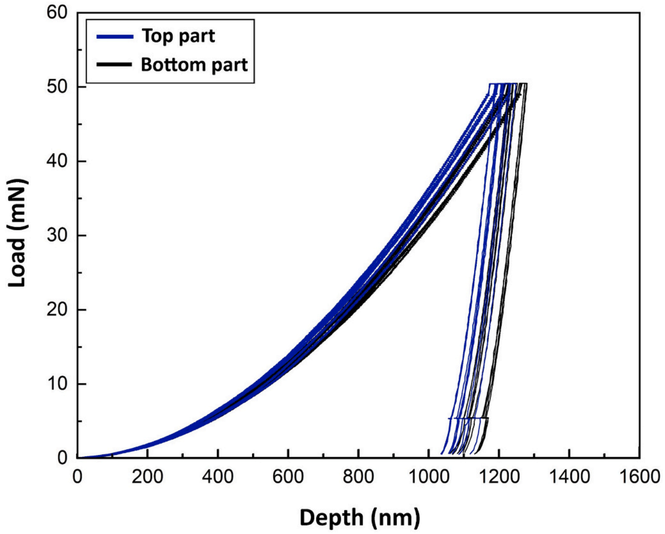

Fig. 7. The load-depth graphs of both samples obtained by the nano-indentation technique.

Comparing different sections of the tensile test samples, the middle area reveals the highest strain magnitude. According to Fig. 12, it is apparently seen that by moving to the sample edges, the equivalent strains decrease. Consequently, it can be assumed that the cracks initiate and propagate from the middle, which subsequently results in failure. The equivalent plastic strain distribution along with the sample length confirms that the top-part sample resists elongation more compared with the bottom-part one. That is the reason behind more strain

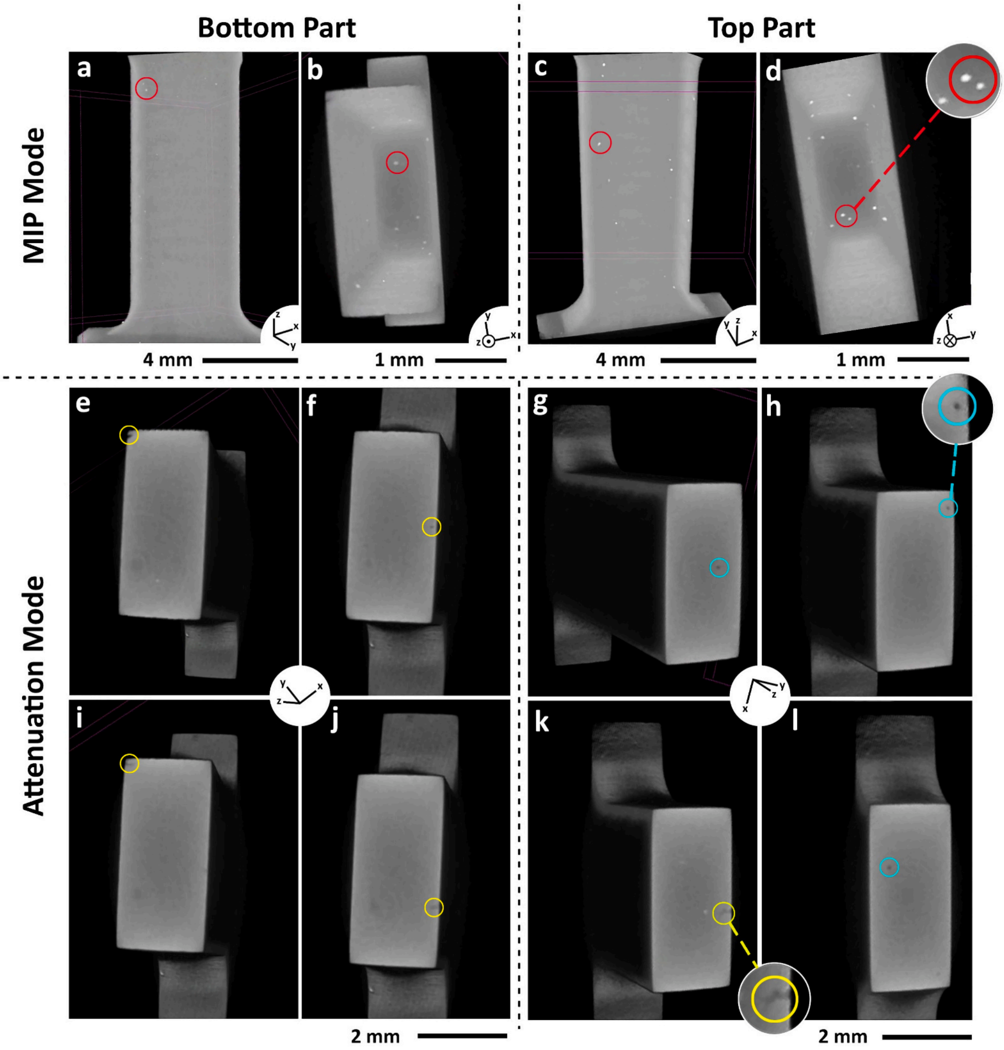

Fig. 8. X-ray micro-CT images of the tensile test samples cut from the bottom-, and the top parts of the LPBF AlSi10Mg (circles in red, yellow, and blue colors point out inclusions, micro-cracks, and porosity, respectively). (For interpretation of the references to color in this figure legend, the reader is referred to the web version of this article.)

Table 7
Mechanical properties of the AM AlSi10Mg samples.

Sample	Property		
	σ_{YS} (MPa) /SD*	σ_{UTS} (MPa) /SD	ε_t
Top part	251.2 / 3.6	473.9 / 4.3	0.071 ± 0.005
Bottom part	221.3 / 2.2	436.3 / 2.7	0.059 ± 0.002

SD: Standard deviation.

accumulation in the middle of the top-part sample than that in similar area of the bottom-part sample.

Stress triaxiality represents the ratio of the mean stress to the equivalent stress [43]. Localization after onset of necking causes an increase in the stress triaxiality. Fig. 13 illustrates the triaxiality magnitudes for both bottom-part and the top-part samples. As shown, the triaxiality of an element in the most critical spot located in the middle of the tensile test samples changes with displacement. Due to a very limited post-necking length observed in Fig. 9, the simulation did not incorporate damage effects, and the results were extrapolated solely from the necking stage until failure. The comparison of material ductility was primarily based on triaxiality and its correlation with the cross-sectional area reduction of the gauge section, albeit acknowledging that other influential factors such as void nucleation and potential void coalescence were not considered. Comparing the stress triaxiality indicates more stress localization in the bottom-part sample. Hence, from the triaxiality and equivalent plastic strain depicted in Fig. 11, it can be concluded that the bottom-part sample is more brittle than the top-part one, which is in good agreement with the uniaxial tensile test results.

6. Discussion

Referring to the aim of this study, which is the effect of distancing from the build plate on the mechanical properties of the AM AlSi10Mg alloy, determining influential factors on the microstructural and physical properties of the component is necessary. According to Figs. 4 and 6, the average cell size and grain size through both parts are reported similar, which indicates that the process parameters *e.g.*, beam power, laser speed, scanning strategy, *etc.* were chosen properly so that the heating/reheating cycles did not affect these features through the building direction. Additionally, the build plate temperature as another important factor affecting the solute concentration and partitioning through the lattice, grain size, and consequently the mechanical properties [44–46], was maintained at a constant level of $200^{\circ}C$ for all experiments. Therefore, the grain-size term in the theoretical strengthening equation, Eq. (1), is ineffectual on variations in tensile properties of the material.

A difference in hardness values in Table 5 implies that the top-part

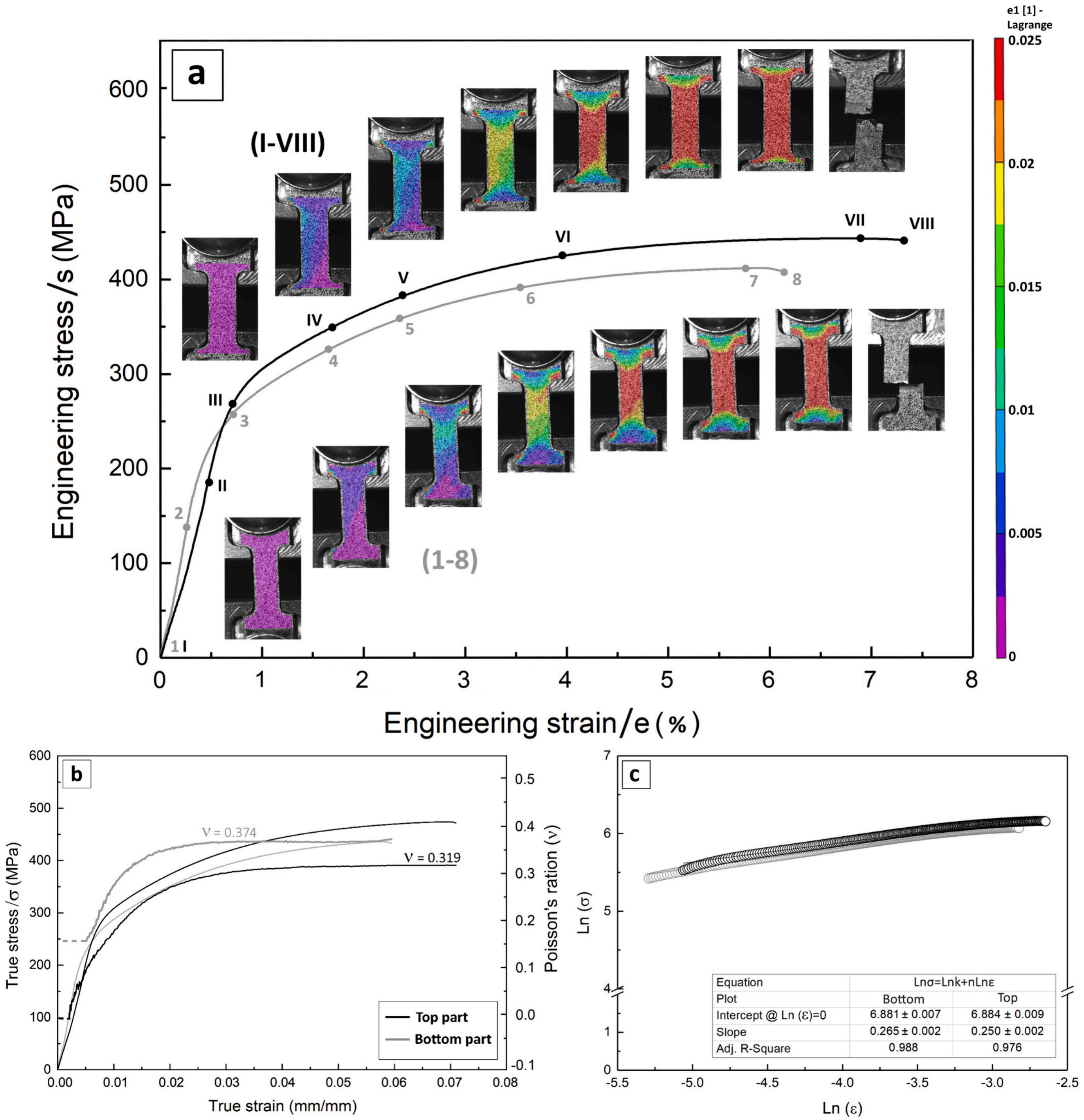

Equation	Lnσ=Lnk+nLnε	
Plot	Bottom	Top
Intercept @ Ln (ε)=0	6.881 ± 0.007	6.884 ± 0.009
Slope	0.265 ± 0.002	0.250 ± 0.002
Adj. R-Square	0.988	0.976

Fig. 9. (a) Engineering stress-strain curves of the top-part and the bottom-part samples, (b) the true stress-strain curves, and the corresponding Poisson's ratio-strain curves, and (c) the strain hardening exponent for both cases (grey: bottom part, black: top part).

sample should show higher strength; however, to confirm that the readings correspond to the matrix, not the precipitates, tensile testing is also needed to be done. Regarding the tensile results, while the stress-strain curves of both samples show almost 35–40 *MPa* and 1.15 % differences in tensile strength and total elongation (*cf.* Fig. 9), the trend of flow curves and $ln\sigma - ln\varepsilon$ curves are comparable. Apart from that, the top part shows a remarkable decrease in the Poisson's ratio when comparing with the bottom part, indicating that the ratio of longitudinal to lateral strains becomes less pronounced as the distance from the build plate increases. While adding silicon into pure aluminum and heat treating the aluminum alloys has been previously shown to reduce Poisson's ratio [47], the presence of a gradient in Poisson's ratio within a single AM component in its as-built state is quite a new phenomenon influenced by multiple factors that require further assessment. Here, the partitioning of Si through the top part, based on the APT results, can be reported as one of the reasons reducing the Poisson's ratio in LPBF AlSi10Mg alloy. However, the intricate nature of the AM process, combined with temperature gradients that result in the formation of various precipitates with varying sizes and morphologies, also need to be considered. All means there should be some factors affecting the tensile properties, not the strain hardenability. This can be attributed to either structural defects *e.g.,* cracks, voids, *etc.*, or solute-induced

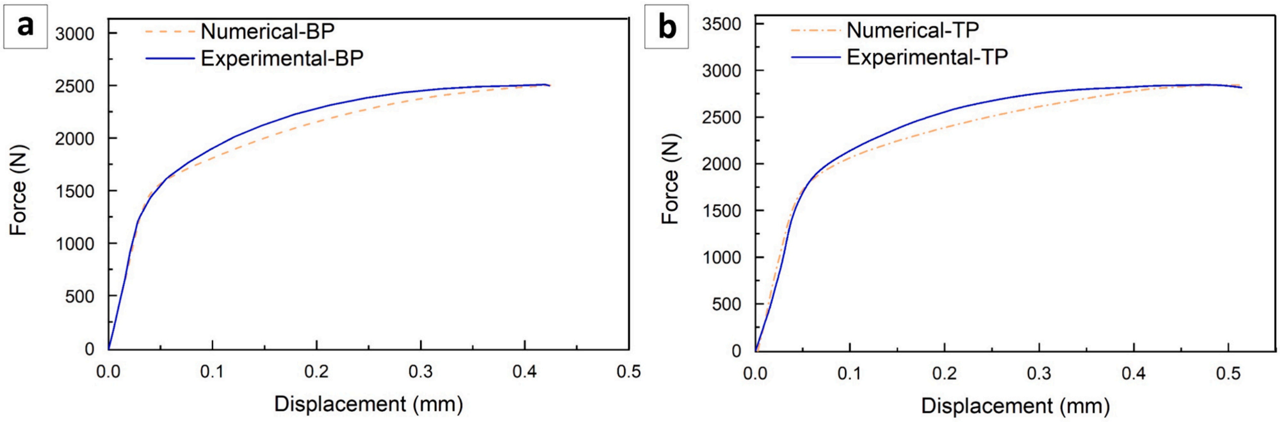

Fig. 10. Verification of 3D-simulated tensile testing in (a) bottom-part, and (b) top-part samples.

Table 8
Constitutive models representing the tensile behavior.

Sample	Plastic strain$\varepsilon \le 0.06$	Plastic strain$\varepsilon > 0.06$
Top part	$K = 59.28 \times 10^3$, $n = 1.05$	$K = 808.14$, $n = 0.20$
Bottom part	$K = 50.77 \times 10^3$, $n = 1.01$	$K = 778.68$, $n = 0.22$

strengthening taken place during the solidification process, or both. Similar trends between the strain hardening rate of both samples in the nanoindentation load-depth curves might recall the fact that the precipitate strengthening should be a determining mechanism causing variations in strength and ductility along the building direction. Regarding that, the term $(\sigma_{Pr} + \sigma_{DW} + \sigma_{GB})$ shows almost 35 MPa difference in its value when we compare both parts. In similar fashion of the grain size which is reported comparable, another research presented similar dislocations' density and dislocation strengthening through the building direction [23,48,49]. Therefore, this difference is probably caused by the difference in precipitation strengthening factor.

According to X-ray micro-CT images (*cf.* Fig. 8), while the bottom-part shows sub-surface microcracking in some areas, the top-part contains microporosity shown within a few cross sections. Besides, both samples present a low volume fraction of inclusions through the bulk. During the AM process, the build plate acts as a heat sink subjecting the

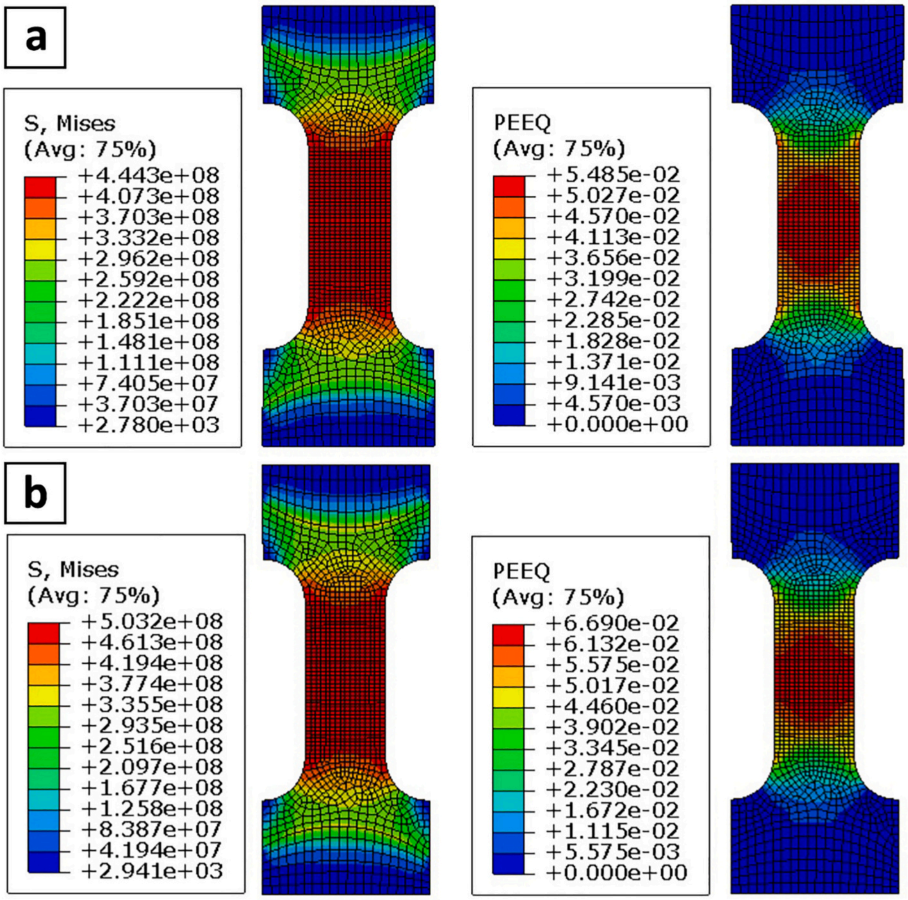

Fig. 11. The Mises stress and the equivalent plastic strain in (a) bottom-part, and (b) top-part samples.

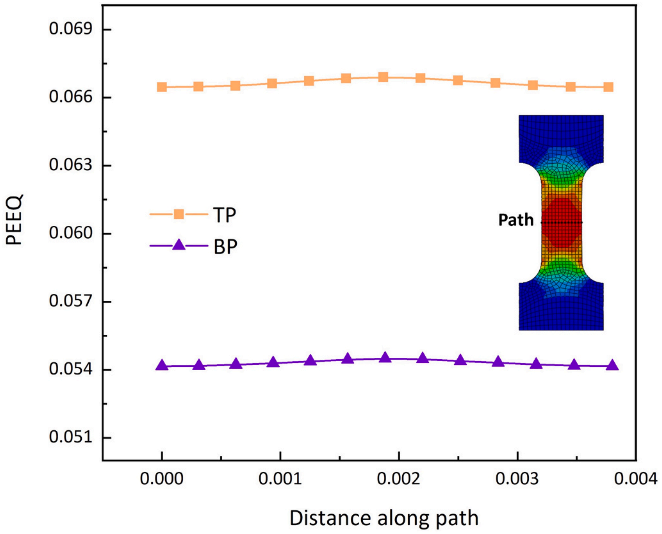

Fig. 12. Variations of the equivalent plastic strain in bottom-part (BP) and top-part (TP) samples.

building product to significant temperature gradients. By distancing from the build plate and due to consecutive heating cycles, the layers already printed keep the heat for longer time that leads to a gentler temperature gradient. On the other side, the heating cycles result in the fusion of the fresh powder layer and partial fusion of a few layers underneath. Gas entrapment and folded oxide films due to interactions between the melt pools and the chamber gas, as well as the melt agitation are usually called porosity resources in AM processing. The dynamic nature of the melt pool from one side, and the partial melting of the last few layers on the other side ease the floatation of trapped low-density gas. While a huge temperature gradient at the beginning which applies thermal-induced residual stresses is mostly responsible for crack formation in the bottom part, upward movement of entrapped gas along the building direction contributes to gas porosity formation through the top part.

Even though the structural defects and their resources are completely different between top and bottom parts, there are no remarkable differences in either the trends of flow curves or the DIC strain contours. Some researchers modeled the brittle and ductile fracture in various crystalline structures and reported that the presence of porosity and micro-void impacts stress triaxiality and failure mode in ductile fracture where void coalescence develops during the post-necking unstable deformation [43,50]. However, pre-cracked samples often show flat to slant fracture transition or a competition between these two modes also called "flip-flap" mechanism, *i.e.,* changing the slant plane orientation during the crack propagation [51,52]. Despite the theoretical differences in failure mechanisms from bottom to top, the flow curves' elastoplastic manner present fair enough similarities, which implicitly notes that the differences in tensile values can be related to the physical properties of the AM material.

According to the TEM analysis in Fig. 3 and the data presented in Table 3, the phases formed during the rapid solidification can be interpreted by considering the partitioning of the alloying elements, faceted/non-faceted growth, and cyclic reheating that facilitates the diffusion. Unlike Mg, Si has proper diffusivity in liquid Al, and consequently low partitioning coefficient, but a huge tendency to grow faceted in liquid Al [53]. While lower k' offers higher potential of partitioning during the solidification, the faceted growth mode is not as frequent as the non-faceted one since it requires potential nucleation sites such as interstitial vacancy, twinning, and screw dislocations [54]. The need for a covalent bond between Si and other elements to form phases also acts as a barrier, which defines it as a time-dependent reaction [55,56]. While the bottom part in contact with the build direction is exposed to a steep temperature gradient, heating/reheating cycles moderate G value that broadens the solidification time.

Through the bottom part but faraway the build plate where fusion/partial fusion of powder layers takes place, Mg and Si atoms have a chance to diffuse within short-range paths to form elongated (Mg,Si)-bearing lamella shown as purple rod-shape precipitates in Fig. 5(b). Although the heat generated by the scanning laser affects a few layers beneath the surface, a steep temperature gradient remains between these layers and those deposited at the very bottom. As a result, the diffusion kinetic is reduced, leading to a lower volume fraction of precipitates in the bottom part compared to the top part. Moreover, there is still a fraction of Mg atoms trapped in the Al matrix since the partitioning coefficient of Mg is high. These atoms are shown as scattered purple dots in TEM Mg-profile of the bottom part. It is worth noting that some of these colonies can be representative of those elongated (Mg,Si)-bearing lamella, which are oriented along with the building direction. Besides, Si with low partitioning coefficient and lower density than Al element can be partitioned through the top layers. On the other side, the top part experiences gentler temperature gradient associated with sufficient diffusion time of solute. As a result, Mg and Si can diffuse and

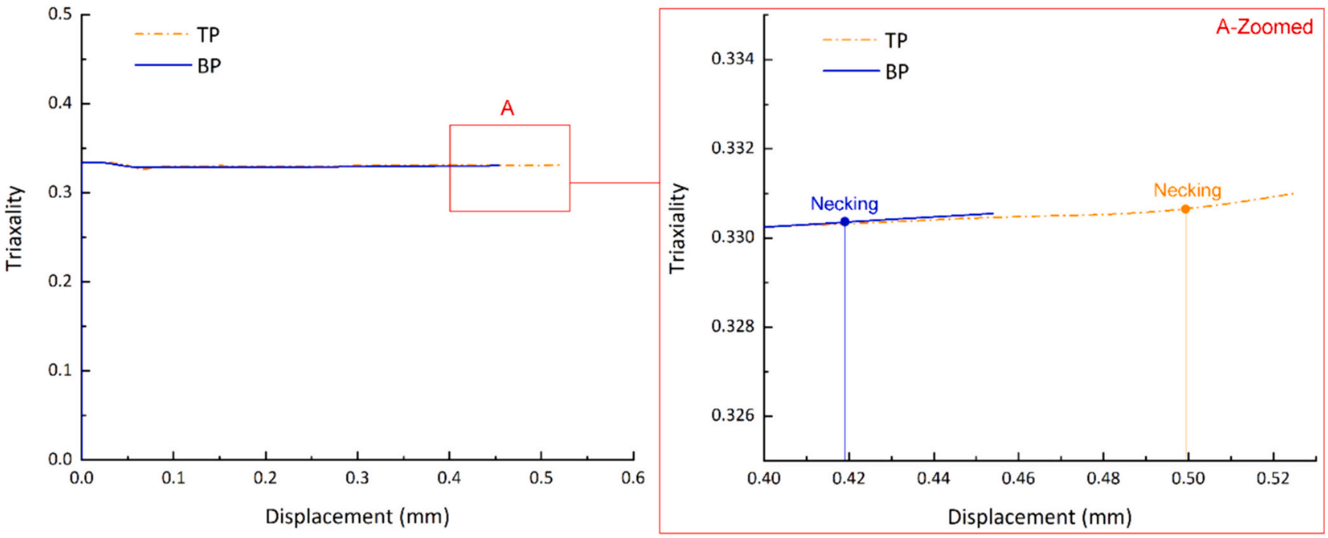

Fig. 13. Variation of the stress triaxiality in the bottom-part (BP) and top-part (TP) samples.

react properly to form high volume fraction of fine (Mg,Si)-bearing precipitates, shown as purple spherical precipitates in Fig. 5(a). Based upon the TEM profiles, the intercellular regions are high-potential sites for nucleation of the eutectic Mg and Si phases. High Si concentration due to its partitioning from the bottom part, as well as sufficient diffusion time facilitates faceted growth of Si-rich blocky phase illustrated in both TEM Si-profile of the top part and APT analysis. The same reason previously mentioned for Mg trapping can be valid through the top part as well. To sum up, while the bottom part suffers from Si depletion, the top part finds a chance to have both faceted Si phase and high fraction of (Mg,Si)-bearing phase due to a gentle temperature gradient and solute enrichment, which is presented in Table 4.

Simulation and experimental force-displacement data show comparable results in which the middle of the samples present the highest equivalent plastic strain magnitudes associated with the high-potential failure area in both samples. Moreover, the distribution of the equivalent strain through the top-part sample shows a higher strain concentration in the middle area compared to the other sample. In addition, the variation of the stress triaxiality in both samples indicates more localization in the bottom-part sample.

Based on all discussed above and the data reported in Table 6, the differences in the tensile strength and the Poisson's ratio of the samples can be attributed to Si partitioning associated with changes in phases chemistry, shape, and geometry, as well as shear modulus and strengthening factors. This factor has a remarkable impact on σ_p, σ_{SS} and σ_{Pr}, while its influence on the strain hardening rate seems to be negligible. Although there are some techniques that can simultaneously increase both strength and elongation such as grain refining, alloy design, microstructure architecting, and heat treatment, the phenomenon reported in this study is quite unexplored. The presence of fine precipitates and better distribution of particles shown in the APT profiles can be other key factors changing the strengthening through the top part. While the laser powder bed fusion can be considered as a self-heat-treating manufacturing process due to consecutive heating-reheating cycles, the complex dynamic nature of this manufacturing process can induce nucleation of further precipitates within the short-range paths due to partial mixing in liquid and no diffusion in solid [9]. Solute trapping/repartitioning during these thermal cycles are reported as an important factor concurrently causing superior strength and ductility. However, to approve this phenomenon as the dominant mechanism, further exploration is required. To the best of knowledge of the authors, there is no other study presenting differences in mechanical behavior of a single AM component, while the grain size is constant through the building direction. This study was trying to recall the importance of other strengthening factors in the total theoretical strengthening equation, particularly at rapid solidification taking place during the laser additive manufacturing. Nonetheless, additional insights can be derived from exploring constitutive models like crystal plasticity, offering potential inspiration for future research studies. To compare, this research provides tensile strength values alongside those from other studies for different AlSiMg alloys, as shown in Table 9.

7. Summary and conclusions

This study showed that by distancing from the build plate, the tensile strength and the total elongation increase in the LPBF AlSi10Mg component vertically printed. To find the reason, the structural integrity, the microstructural features, and the thermophysical properties during rapid solidification were investigated. The results can be summarized as follows:

- While the microstructural analysis showed similar average grain size, the micro-CT analysis revealed lack of structural integrity in a few cross sections containing microcracks and porosity through the bottom part and the top part, respectively.

Table 9
A comparison between mechanical properties of the AlSiMg alloys produced using various manufacturing techniques and heat treatment processes.

Study	Material/condition	σ_{YS} (MPa) /SD*	σ_{UTS} (MPa) /SD	ε_t	n	ϑ
Current	As-built LPBF AlSi10Mg (top part)	251.2 / 3.6	473.9 / 4.3	0.071 ± 0.005	0.25	0.319 ± 0.007
	As-built LPBF AlSi10Mg (bottom part)	221.3 / 2.2	436.3 / 2.7	0.059 ± 0.002	0.26	0.374 ± 0.004
Lutz and Huber [57]	As-built LPBF AlSi10Mg (vertical)	238 / 4.2	429 / 12.6	0.051 ± 0.009	–	–
	Annealed LPBF (360$^{\circ}C$/60 min) AlSi10Mg (vertical)	127 / 2.3	228 / 2.0	0.204 ± 0.012	–	–
	Annealed LPBF (360$^{\circ}C$/60 min) AlSi10Mg (horizontal)	136 / 2.9	229 / 0.8	0.241 ± 0.01	–	–
	As-built LPBF AlSi3.5 Mg2.5 (vertical)	271 / 3.4	407 / 2.4	0.081 ± 0.007	–	–
	Annealed LPBF (360$^{\circ}C$/60 min) AlSi3.5 Mg2.5 (vertical)	111 / 1.0	190 / 0.8	0.267 ± 0.013	–	–
	Annealed LPBF (360$^{\circ}C$/60 min) AlSi3.5 Mg2.5 (horizontal)	112 / 0.9	184 / 1.4	0.247 ± 0.013	–	–
Li et al. [58]	As-built LPBF AlSi10Mg	322.2 / 8.1	434.2 / 10.7	0.053 ± 0.002	–	–
	Heat-treated LPBF (450$^{\circ}C$/120 min) AlSi10Mg (vertical)	196.6 / 3.6	282.4 / 6.1	0.134 ± 0.005	–	–
	Heat-treated LPBF (550$^{\circ}C$/120 min) AlSi10Mg (vertical)	90.5 / 1.6	168.1 / 2.4	0.237 ± 0.008	–	–
Ming et al. [59]	As-built LPBF AlSi7Mg	213 /1	379 / 1.2	0.179 ± 0.008	0.23	–
	Direct-aged LPBF (160$^{\circ}C$/10 h/air cooled) AlSi7Mg	236 / 1	383 / 1	0.138 ± 0.012	0.20	–
	Annealed LPBF (300$^{\circ}C$/1.5 h/air cooled) AlSi7Mg	171 / 2	269 / 1.5	0.17 ± 0.02	0.17	–
	Solution-aged LPBF (525$^{\circ}C$/0.25 h/water cooled >160$^{\circ}C$/10 h/air cooled) AlSi7Mg	137 / 2.6	218 / 2.3	0.219 ± 0.024	0.16	–
Li et al. [60]	As-built LPBF AlSi10Mg	264 / 4	454 / 5	0.078 ± 0.007	0.26	–
	As-cast LPBF AlSi10Mg	99	170	0.04	0.20	–
	Heat-treated (T6) cast AlSi10Mg	250	320	0.057	0.1	–
Sert et al. [61]	As-built LPBF AlSi7Mg (BD: 0̊ - horizontal)	226.1 / 8.1	352.1 / 8.9	0.052 ± 0.005	–	0.371 ± 0.011

(continued on next page)

Table 9 (*continued*)

Study	Material/ condition	σ_{YS} ($\boldsymbol{MPa}$) /SD*	σ_{UTS} ($\boldsymbol{MPa}$) /SD	ε_t	$\boldsymbol{n}$	ϑ
	As-built LPBF AlSi7Mg (BD*: 45°)	190.1 / 4.0	322.6 / 3.6	0.044 ± 0.003	–	0.332 ± 0.048
	As-built LPBF AlSi7Mg (BD: 60°)	205.7 / 5.4	348.4 / 6.4	0.043 ± 0.003	–	0.385 ± 0.030
	As-built LPBF AlSi7Mg (BD: 70°)	201.4 / 7.1	356.6 / 10.2	0.042 ± 0.002	–	0.309 ± 0.043
	As-built LPBF AlSi7Mg (BD: 80°)	188.1 / 5.1	344.3 / 6.6	0.045 ± 0.002	–	0.341 ± 0.019
	As-built LPBF AlSi7Mg (BD: 90° - vertical)	185.9 / 3.9	344.8 / 5.9	0.048 ± 0.002	–	0.389 ± 0.008
	LPBF AlSi7Mg powder	227 / 11	397 / 11	0.06 ± 0.01	–	–
Caceres and Selling [62]	Heat-treated (T6) cast AlSi7Mg0.4	–	–	~ 0.10 ± 0.01 (@ 0.2 % porosity)	0.1	–

BD: Building direction.

- The top part presented higher hardness and cumulative strain energy that was not grain-size dependent; however, trend of the strain hardening rate in both samples, obtained by the nanoindentation, followed a similar trend indicating that the nature of structural defects, *i.e.,* stress-induced cracking or porosity due to gas entrapment, was not a dominant factor applying variations in the tensile properties. The Poisson's ratio also showed a meaningful difference between the top and bottom parts, emphasizing the importance of phases formation and distribution on the relationship between longitudinal and lateral strains.
- The TEM and the APT results indicated that both top and bottom parts show (Mg,Si)-bearing phases but with different size and morphology. The top part contains blocky Si-rich phase thanks to Si partitioning during the heating/reheating cycles. The rest of the Mg atoms experienced either participation in Mg-Si reaction to form the (Mg,Si)-bearing phase or trapping phenomenon through the entire matrix. The differences in solute partitioning and phase formation were reported as dominant factors changing the hardness, elastic, and shear moduli, strengthening mechanism, and subsequently tensile properties.
- According to the simulation results, it was found that in both samples, the plastic strains were accumulated in the middle of the gauge introducing potential zones of fracture initiation. Moreover, since the top part showed higher magnitude of stress triaxiality all while an equivalent plastic strain, this sample presented more localization during the tensile testing.

CRediT authorship contribution statement

A. Asgari: Writing – original draft, Investigation, Formal analysis, Data curation. **B. Shalchi Amirkhiz:** Writing – review & editing, Formal analysis, Data curation. **B. Langelier:** Writing – review & editing, Formal analysis, Data curation. **A. Hadadzadeh:** Writing – review & editing, Formal analysis, Data curation. **A. Lloyd:** Writing – review & editing, Formal analysis, Data curation. **M. Mohammadi:** Writing – original draft, Methodology, Investigation, Formal analysis, Conceptualization.

Declaration of competing interest

The authors declare no conflict of interest. Also, they have no competing financial interests or personal relationships that could have appeared to influence the work reported in this paper.

Data availability

Data will be made available on request.

Acknowledgement

The Authors would like to thank the funding provided by Atlantic Canada Opportunities Agency (ACOA)-Atlantic Innovation Fund project number 210414 to complete this work. The authors would like to acknowledge Steven R. Cogswell, and Navid Hasani for the experimental support.

References

[1] W. Kurz, B. Giovanola, R. Trivedi, Theory of microstructural development during rapid solidification, Acta Metall. 34 (1986) 823–830, https://doi.org/10.1016/0001-6160(86)90056-8.

[2] L.A. Jacobson, J. Mckittrick, Rapid solidification processing, Mater. Sci. Eng. R 11 (1994) 355–408, https://doi.org/10.1016/0927-796X(94)90022-1.

[3] H. Qin, Q. Dong, V. Fallah, M.R. Daymond, Rapid solidification and non-equilibrium phase constitution in laser powder bed fusion (LPBF) of AlSi10Mg alloy: analysis of nano-precipitates, eutectic phases, and hardness evolution, Metall. Mater. Trans. A Phys. Metall. Mater. Sci. 51 (2020) 448–466, https://doi.org/10.1007/s11661-019-05505-5.

[4] M. Fousová, D. Dvorský, A. Michalcová, D. Vojtěch, Changes in the microstructure and mechanical properties of additively manufactured AlSi10Mg alloy after exposure to elevated temperatures, Mater. Charact. 137 (2018) 119–126, https://doi.org/10.1016/j.matchar.2018.01.028.

[5] T. DebRoy, H.L. Wei, J.S. Zuback, T. Mukherjee, J.W. Elmer, J.O. Milewski, A. M. Beese, A. Wilson-Heid, A. De, W. Zhang, Additive manufacturing of metallic components – process, structure and properties, Prog. Mater. Sci. 92 (2018) 112–224, https://doi.org/10.1016/j.pmatsci.2017.10.001.

[6] D. Hu, N. Grilli, L. Wang, M. Yang, W. Yan, Microscale residual stresses in additively manufactured stainless steel: computational simulation, J. Mech. Phys. Solids 161 (2022) 104822, https://doi.org/10.1016/J.JMPS.2022.104822.

[7] C. Butler, S. Babu, R. Lundy, R. O'Reilly Meehan, J. Punch, N. Jeffers, Effects of processing parameters and heat treatment on thermal conductivity of additively manufactured AlSi10Mg by selective laser melting, Mater. Charact. 173 (2021) 110945, https://doi.org/10.1016/j.matchar.2021.110945.

[8] A. Martin, M. Vilanova, E. Gil, M.S. Sebastian, C.Y. Wang, S. Milenkovic, M. T. Pérez-Prado, C.M. Cepeda-Jiménez, Influence of the Zr content on the processability of a high strength Al-Zn-mg-cu-Zr alloy by laser powder bed fusion, Mater. Charact. 183 (2022), https://doi.org/10.1016/j.matchar.2021.111650.

[9] M.H. Ghoncheh, M. Sanjari, A.S. Zoeram, E. Cyr, B.S. Amirkhiz, A. Lloyd, M. Haghshenas, M. Mohammadi, On the microstructure and solidification behavior of new generation additively manufactured Al-cu-mg-ag-Ti-B alloys, Addit. Manuf. 37 (2021), https://doi.org/10.1016/j.addma.2020.101724.

[10] M.H. Ghoncheh, M. Sanjari, E. Cyr, J. Kelly, H. Pirgazi, S. Shakerin, A. Hadadzadeh, B.S. Amirkhiz, L.A.I. Kestens, M. Mohammadi, On the solidification characteristics, deformation, and functionally graded interfaces in additively manufactured hybrid aluminum alloys, Int. J. Plast. 133 (2020), https://doi.org/10.1016/j.ijplas.2020.102840.

[11] X. Tong, G. Wu, M.A. Easton, M. Sun, Q. Wang, L. Zhang, Microstructural evolution and strengthening mechanism of mg-Y-RE-Zr alloy fabricated by quasi-directed energy deposition, Addit. Manuf. 67 (2023) 103487, https://doi.org/10.1016/j.addma.2023.103487.

[12] X.X. Zhang, A. Lutz, H. Andrä, M. Lahres, W.M. Gan, E. Maawad, C. Emmelmann, Evolution of microscopic strains, stresses, and dislocation density during in-situ tensile loading of additively manufactured AlSi10Mg alloy, Int. J. Plast. 139 (2021), https://doi.org/10.1016/j.ijplas.2021.102946.

[13] K. Kempen, L. Thijs, J. Van Humbeeck, J.P. Kruth, Mechanical properties of AlSi10Mg produced by selective laser melting, Phys. Procedia 39 (2012) 439–446, https://doi.org/10.1016/j.phpro.2012.10.059.

[14] I. Rosenthal, R. Shneck, A. Stern, Heat treatment effect on the mechanical properties and fracture mechanism in AlSi10Mg fabricated by additive manufacturing selective laser melting process, Mater. Sci. Eng. A 729 (2018) 310–322, https://doi.org/10.1016/j.msea.2018.05.074.

[15] I. Rosenthal, A. Stern, N. Frage, Microstructure and mechanical properties of AlSi10Mg parts produced by the laser beam additive manufacturing (AM) technology, Metallography, Microstructure, and Analysis 3 (2014) 448–453, https://doi.org/10.1007/s13632-014-0168-y.

[16] D.M. Stefanescu, Science and engineering of casting solidification, Third edition, 2015, https://doi.org/10.1007/978-3-319-15693-4.

[17] E.L. Huskins, B. Cao, K.T. Ramesh, Strengthening mechanisms in an Al-mg alloy, Mater. Sci. Eng. A 527 (2010) 1292–1298, https://doi.org/10.1016/j.msea.2009.11.056.

[18] K.L. Kendig, D.B. Miracle, Strengthening Mechanisms of an Al-mg-Sc-Zr Alloy. www.actamat-journals.com, 2002.

[19] N.J. Harrison, I. Todd, K. Mumtaz, Reduction of micro-cracking in nickel superalloys processed by selective laser melting: a fundamental alloy design approach, Acta Mater. 94 (2015) 59–68, https://doi.org/10.1016/j.actamat.2015.04.035.

[20] T. Gancarz, A. Dobosz, A.A. Bogno, G. Cempura, N. Schell, R. Chulist, H. Henein, Characterization of rapidly solidified Al-mg-Sc alloys with Li addition, Mater. Charact. 178 (2021) 111290, https://doi.org/10.1016/j.matchar.2021.111290.

[21] A. Hadadzadeh, B.S. Amirkhiz, B. Langelier, J. Li, M. Mohammadi, Microstructural consistency in the additive manufactured metallic materials: a study on the laser powder bed fusion of AlSi10Mg, Addit. Manuf. 46 (2021), https://doi.org/10.1016/j.addma.2021.102166.

[22] X.X. Zhang, D. Knoop, H. Andrä, S. Harjo, T. Kawasaki, A. Lutz, M. Lahres, Multiscale constitutive modeling of additively manufactured Al-Si-Mg alloys based on measured phase stresses and dislocation density, Int. J. Plast. 140 (2021), https://doi.org/10.1016/j.ijplas.2021.102972.

[23] A. Hadadzadeh, C. Baxter, B.S. Amirkhiz, M. Mohammadi, Strengthening mechanisms in direct metal laser sintered AlSi10Mg: comparison between virgin and recycled powders, Addit. Manuf. 23 (2018) 108–120, https://doi.org/10.1016/j.addma.2018.07.014.

[24] M.E. Glicksman, Principles of solidification: an introduction to modern casting and crystal growth concepts, Springer, 2010, https://doi.org/10.1007/978-1-4419-7344-3.

[25] P. Mohammadpour, A. Plotkowski, A.B. Phillion, Revisiting solidification microstructure selection maps in the frame of additive manufacturing, Addit. Manuf. 31 (2020), https://doi.org/10.1016/j.addma.2019.100936.

[26] R.W. Hertzberg, Deformation and Fracture Mechanics of Engineering Materials, J, Wiley & Sons, 1996.

[27] R.E. Peierls, Proc. Phys. Soc. 52 (1940) 34.

[28] A. Simar, Y. Bréchet, B. de Meester, A. Denquin, T. Pardoen, Sequential modeling of local precipitation, strength and strain hardening in friction stir welds of an aluminum alloy 6005A-T6, Acta Mater. 55 (2007) 6133–6143, https://doi.org/10.1016/j.actamat.2007.07.012.

[29] J.G. Santos Macías, T. Douillard, L. Zhao, E. Maire, G. Pyka, A. Simar, Influence on microstructure, strength and ductility of build platform temperature during laser powder bed fusion of AlSi10Mg, Acta Mater. 201 (2020) 231–243, https://doi.org/10.1016/j.actamat.2020.10.001.

[30] K. Khan, L. Srinivasa Mohan, A. De, T. DebRoy, Rapid calculation of part scale residual stress – powder bed fusion of stainless steel, and aluminum, titanium, nickel alloys, Addit. Manuf. 60 (2022), https://doi.org/10.1016/j.addma.2022.103240.

[31] B.L. Silva, I.J.C. Araujo, W.S. Silva, P.R. Goulart, A. Garcia, J.E. Spinelli, Correlation between dendrite arm spacing and microhardness during unsteady-state directional solidification of Al-Ni alloys, Philos. Mag. Lett. 91 (2011) 337–343, https://doi.org/10.1080/09500839.2011.559911.

[32] M.A. Kearns, P.S. Cooper, Effects of solutes on grain refinement of selected wrought aluminium alloys, mater, Sci. Technol. 13 (1997) 650–654, https://doi.org/10.1179/mst.1997.13.8.650.

[33] P. Desnaint, Y. Fautrelle, J.-L. Meyer, J.-P. Riquet, F. Durand, Prediction of equiaxed grain density in multicomponent alloys, stirred electromagnetically, Acta Metall. Mater. 38 (1990) 1513–1523, https://doi.org/10.1016/0956-7151(90)90119-2.

[34] J.P. Garandet, G. Mathiak, V. Botton, P. Lehmann, A. Griesche, Reference microgravity measurements of liquid phase solute diffusivities in tin-and aluminum-based alloys, Int. J. Thermophys. 25 (2004), https://doi.org/10.1023/B:IJOT.0000022338.21866.f9.

[35] F.R.N. Nabarro, Theoretical and experimental estimates of the peierls stress, Philos. Mag. 75 (1997) 703–711, https://doi.org/10.1080/01418619708207197.

[36] M.A. Bhatia, M. Azarnoush, I. Adlakha, G. Lu, K.N. Solanki, Dislocation core properties of β-tin: a first-principles study, Model. Simul. Mater. Sci. Eng. 25 (2017), https://doi.org/10.1088/1361-651X/aa57d0.

[37] Y. Gao, A Peierls perspective on mechanisms of atomicfriction, J. Mech. Phys. Solids 58 (2010) 2023–2032, https://doi.org/10.1016/J.JMPS.2010.09.014.

[38] G.J. Nie, R.C. Batra, Exact solutions and material tailoring for functionally graded hollow circular cylinders, J. Elast. 99 (2010) 179–201, https://doi.org/10.1007/s10659-009-9239-8.

[39] M. Mohammadi, J.R. Dryden, L. Jiang, Stress concentration around a hole in a radially inhomogeneous plate, Int. J. Solids Struct. 48 (2011) 483–491, https://doi.org/10.1016/j.ijsolstr.2010.10.013.

[40] M. Mohammadi, J.R. Dryden, Influence of the spatial variation of Poisson's ratio upon the elastic field in nonhomogeneous axisymmetric bodies, Int. J. Solids Struct. 46 (2009) 788–795, https://doi.org/10.1016/j.ijsolstr.2008.09.030.

[41] M. Mohammadi, A.P. Brahme, R.K. Mishra, K. Inal, Effects of post-necking hardening behavior and equivalent stress–strain curves on the accuracy of M–K based forming limit diagrams, Comput. Mater. Sci. 85 (2014) 316–323, https://doi.org/10.1016/J.COMMATSCI.2014.01.017.

[42] E.V. Fomin, A.E. Mayer, Slip of low-angle tilt grain boundary (110) in FCC metals at perpendicular shear, Int. J. Plast. 134 (2020) 102843, https://doi.org/10.1016/J.IJPLAS.2020.102843.

[43] A. Pineau, A.A. Benzerga, T. Pardoen, Failure of metals I: brittle and ductile fracture, Acta Mater. 107 (2016) 424–483, https://doi.org/10.1016/j.actamat.2015.12.034.

[44] P. Van Cauwenbergh, V. Samaee, L. Thijs, J. Nejezchlebová, P. Sedlák, A. Iveković, D. Schryvers, B. Van Hooreweder, K. Vanmeensel, Unravelling the multi-scale structure–property relationship of laser powder bed fusion processed and heat-treated AlSi10Mg, Sci. Rep. 11 (2021) 1–15, https://doi.org/10.1038/s41598-021-85047-2.

[45] E. Cerri, E. Ghio, G. Bolelli, Effect of the distance from build platform and post-heat treatment of AlSi10Mg alloy manufactured by single- and multi-laser selective laser melting, J. Mater. Eng. Perform. 30 (2021) 4981–4992, https://doi.org/10.1007/s11665-021-05577-8.

[46] S. Zhu, I. Katti, D. Qiu, J.H. Forsmark, M.A. Easton, Microstructural analysis of the influences of platform preheating and post-build heat treatment on mechanical properties of laser powder bed fusion manufactured AlSi10Mg alloy, Mater. Sci. Eng. A 882 (2023) 145486, https://doi.org/10.1016/j.msea.2023.145486.

[47] W. Koster, H. Franz, Poisson's ratio for metals and alloys, Metallurgical Reviews 6 (1961) 1–56, https://doi.org/10.1179/mtlr.1961.6.1.1.

[48] Z. Li, Z. Li, Z. Tan, D.B. Xiong, Q. Guo, Stress relaxation and the cellular structure-dependence of plastic deformation in additively manufactured AlSi10Mg alloys, Int. J. Plast. 127 (2020), https://doi.org/10.1016/j.ijplas.2019.12.003.

[49] M. Lindroos, T. Pinomaa, K. Ammar, A. Laukkanen, N. Provatas, S. Forest, Dislocation density in cellular rapid solidification using phase field modeling and crystal plasticity, Int. J. Plast. 148 (2022) 103139, https://doi.org/10.1016/J.IJPLAS.2021.103139.

[50] R. Muro-Barrios, Y. Cui, J. Lambros, H.B. Chew, Dual-scale porosity effects on crack growth in additively manufactured metals: 3D ductile fracture models, J. Mech. Phys. Solids 159 (2022) 104727, https://doi.org/10.1016/J.JMPS.2021.104727.

[51] T. Pardoen, F. Hachez, B. Marchioni, P.H. Blyth, A.G. Atkins, Mode I fracture of sheet metal, J. Mech. Phys. Solids 52 (2004) 423–452, https://doi.org/10.1016/S0022-5096(03)00087-5.

[52] S.A. El-Naaman, K.L. Nielsen, Observations on mode I ductile tearing in sheet metals, European Journal of Mechanics, A/Solids 42 (2013) 54–62, https://doi.org/10.1016/j.euromechsol.2013.04.007.

[53] A.J. Shahani, X. Xiao, K. Skinner, M. Peters, P.W. Voorhees, Ostwald ripening of faceted Si particles in an Al-Si-cu melt, Mater. Sci. Eng. A 673 (2016) 307–320, https://doi.org/10.1016/j.msea.2016.06.077.

[54] L. Ratke, P. Voorhees, Growth and coarsening: Ostwald ripening in material processing, springer-Verlag, Berlin Heidelberg GmbH Engineering (2002), https://doi.org/10.1080/08940886.2017.1316123.

[55] G. Kurtuldu, P. Jarry, M. Rappaz, Influence of icosahedral short range order on diffusion in liquids: a study on Al-Zn-Cr alloys, Acta Mater. 115 (2016) 423–433, https://doi.org/10.1016/j.actamat.2016.05.051.

[56] I. Han, X. Xiao, H. Sun, A.J. Shahani, A side-by-side comparison of the solidification dynamics of quasicrystalline and approximant phases in the Al–co–Ni system, Acta Crystallographica A: Foundations and Advances 75 (2019) 281–296, https://doi.org/10.1107/S2053273318017114.

[57] A. Lutz, L. Huber, Strain-rate dependent material properties of selective laser melted AlSi10Mg and AlSi3.5Mg2.5, Materialpruefung/Materials Testing 62 (2020) 573–583, https://doi.org/10.3139/120.111518.

[58] C. Li, W.X. Zhang, H.O. Yang, J. Wan, X.X. Huang, Y.Z. Chen, Microstructural origin of high strength and high strain hardening capability of a laser powder bed fused AlSi10Mg alloy, J. Mater. Sci. Technol. 197 (2024) 194–206, https://doi.org/10.1016/j.jmst.2024.01.067.

[59] X. Ming, D. Song, A. Yu, H. Tan, Q. Zhang, Z. Zhang, J. Chen, X. Lin, Effect of heat treatment on microstructure, mechanical and thermal properties of selective laser melted AlSi7Mg alloy, J. Alloys Compd. 945 (2023) 169278, https://doi.org/10.1016/j.jallcom.2023.169278.

[60] W. Li, S. Li, J. Liu, A. Zhang, Y. Zhou, Q. Wei, C. Yan, Y. Shi, Effect of heat treatment on AlSi10Mg alloy fabricated by selective laser melting: microstructure evolution, mechanical properties and fracture mechanism, Mater. Sci. Eng. A 663 (2016) 116–125, https://doi.org/10.1016/j.msea.2016.03.088.

[61] E. Sert, E. Schuch, A. Öchsner, L. Hitzler, E. Werner, M. Merkel, Tensile strength performance with determination of the Poisson‘s ratio of additively manufactured AlSi10Mg samples, Mater. Werkst. 50 (2019) 539–545, https://doi.org/10.1002/mawe.201800233.

[62] C.H. Cáceres, B.I. Selling, Casting defects and the tensile properties of an Al-Si-Mg alloy, Mater. Sci. Eng. A 220 (1996) 109–116, https://doi.org/10.1016/S0921-5093(96)10433-0.